

On the Interplay between Size and Disorder in Suppressing Intercalation-Induced Phase Transitions in Pseudocapacitive Nanostructured MoS₂

Yiyi Yao,^a Helen Cumberbatch,^a Daniel D. Robertson,^a Matthew A. Chin,^b Ryan Lamkin,^a and Sarah H. Tolbert*^{a,b,c}

^a Department of Chemistry and Biochemistry, UCLA, Los Angeles, California 90095-1569, U.S.A.

^b Department of Materials Science and Engineering, UCLA, Los Angeles, California 90095-1595, U.S.A.

^c The California NanoSystems Institute, UCLA, Los Angeles, California 90095, U.S.A.

*Corresponding Author. E-mail: tolbert@chem.ucla.edu

Keywords: molybdenum disulfide, mesoporous, operando xrd, pair distribution function analysis, disorder, pseudocapacitance, kinetic analysis

Abstract:

Pseudocapacitors are an emerging class of energy storage materials that offer an attractive compromise between the energy density of batteries and power density of electric double-layer capacitors. Decreasing particle size and increasing surface area of battery materials is a common approach for introducing pseudocapacitive behavior and increasing power density. However, in many cases, as the crystal size is reduced, lattice disorder of unknown extent is also introduced, making it difficult to untangle the relative contribution of size and disorder to fast-charging performance. In this work, a series of nanostructured MoS₂ structures were synthesized with different crystallite sizes and degrees of crystallinity to decouple the effects of size and disorder on charge/discharge kinetics. The extent and type of disorder in each material was quantified by total x-ray scattering experiments and pair distribution function analyses. Electrochemical characterization, including galvanostatic rate capability, cyclic voltammetry, and various kinetic analyses, were used to demonstrate that both decreasing particle size and introducing lattice disorder are effective strategies for increasing charge storage kinetics, and that the effects are additive. Finally, *operando* X-ray diffraction measurements showed that both size and disorder can be used to suppress first-order Li intercalation-induced phase transitions, a key feature for enabling pseudocapacitive charge storage.

This is the author manuscript accepted for publication and has undergone full peer review but has not been through the copyediting, typesetting, pagination and proofreading process, which may lead to differences between this version and the [Version of Record](#). Please cite this article as [doi: 10.1002/adfm.202304896](https://doi.org/10.1002/adfm.202304896).

This article is protected by copyright. All rights reserved.

1. Introduction

As we move towards replacing traditional combustion engine-based vehicles with electric vehicles (EVs), some drawbacks inhibiting widespread usage of EVs are the short driving range and long charging times.¹ These limitations are a direct result of the slow Li-ion diffusion rate in bulk battery materials. Li-ion batteries (LIB) reach full charge within hours but re-fueling a gasoline-powered vehicle takes only minutes. This disparity highlights the need for energy storage devices that can support both high energy density and power density. A class of materials that are attracting increasing interest are pseudocapacitors. These materials utilize Faradaic redox reactions and thus offer higher energy density than electric double layer capacitors (EDLCs), while simultaneously providing higher power density than standard LIB materials, by employing surface or near-surface redox sites.²⁻⁶

Conventional LIB materials store charge through Faradaic redox reactions occurring in the entire bulk material. This mechanism affords high energy density, but the power density is limited by slow solid-state Li^+ diffusion. In many materials, as Li^+ is inserted, at some critical Li^+ concentration, a first-order phase transformation occurs between the Li-poor and Li-rich phases.⁷⁻⁹ The intercalation-induced phase transformation requires symmetry breaking and large rearrangements of the crystal lattice and limits kinetic performance since the Li^+ diffusion rate is linked to the movement of the phase boundary. Repeated charging and discharging with large structural changes also induce stress in the material and long-term capacity fade.

Pseudocapacitors also store charge through redox reactions, but the rate performance is no longer limited by semi-infinite diffusion.¹⁰ This can often be achieved by nanostructuring a battery material so that more redox occurs near the surface and ion diffusion lengths are shortened. As a result, the material can charge within minutes, and the electrical response of a pseudocapacitive material more closely resembles that of a capacitor. This can be observed in a plot of the voltage vs. charge stored during galvanostatic cycling (GV), where a capacitor shows a linear response as function of charge, while a battery material exhibits voltage plateaus at the redox potential where a phase transformation occurs. These two mechanisms can also be distinguished in the cyclic voltammogram (CV), where a battery material shows large peak currents near the redox potentials but little current elsewhere in the potential window. In contrast, a capacitor shows a broad current response throughout the entire voltage window, resulting in a more “box-like” CV. A pseudocapacitive material often exhibits a pseudo-linear GV curve, indicating lack of intercalation-induced phase transitions, and a nearly rectangular CV with significantly broadened redox peaks.

This article is protected by copyright. All rights reserved.

Therefore, a pseudocapacitor utilizes the charge storage mechanism of a battery while demonstrating electrochemical performance similar to a capacitor.¹¹ Most importantly, an essential structural feature of pseudocapacitive materials is the suppression of first-order phase transition upon Li (de-)intercalation due to the kinetic limitations associated with such transitions.⁹⁻¹⁵

Numerous studies have shown that by decreasing the crystallite size of conventional battery materials, pseudocapacitive charge storage (or fast-charging rate performance) can be achieved in materials such as LiCoO_2 ,¹⁶ MoO_2 ,^{17,18} TiS_2 ,^{13,19} nanocrystal MoS_2 ,^{20,21} and others.^{22,23} In an ion intercalation host, the diffusion coefficient, D , is related to the diffusion length, L , by the time constant, τ_d , which represents a characteristic time scale for diffusion (Equation 1).

$$\tau_d = \frac{L^2}{D} \quad (1)$$

Decreasing the crystal size effectively shortens the diffusion length that intercalating ions must travel, thereby speeding up the charging and discharging time. In the absence of a phase transition, the diffusion coefficient is the kinetic rate constant for Li hopping through lattice sites and can be expressed as a function of the hopping activation energy barrier.^{24,25}

$$D = D_0 e^{\frac{-E_a}{k_B T}} \quad (2)$$

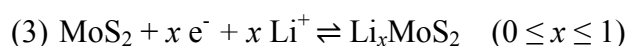
However, when a Li^+ intercalation-induced phase transition occurs, this intrinsic diffusion constant becomes tied to the movement of the phase boundary rather than the Li^+ ion. Therefore, the phase transition limits the diffusion rate. To increase the diffusion coefficient, we also consider material design principles that modify the energy landscape and lower the barrier for traversing the crystal structure.

One strategy is to intentionally incorporate disorder into the crystal. For example, cation disorder in otherwise fully crystalline anode materials has been computationally found to increase performance as it results in local Li environments differing from one unit cell to the next, suppressing long-range lithium ion ordering and offering multiple site/pathway options for intercalating Li ions.²⁶ A large number of the fastest currently known bulk anode materials are such innately cation disordered materials such as Wadsley-Roth shear phases or mixed metal oxide bronze phases.^{27,28} Similarly, cation and vacancy disorder have been observed to increase Li-ion conductivity in solid-state electrolytes by reducing the energetic barriers along diffusion pathways.^{29,30} Another extensively studied example of this approach is the development of the fast-charging layered cathode material, $\text{LiNi}_{0.80}\text{Co}_{0.15}\text{Al}_{0.05}\text{O}_2$ (NCA), from parent structures LiNiO_2 and

This article is protected by copyright. All rights reserved.

LiCoO₂ by introducing substitutional disorder in the form of cation dopants.^{31,32} Both LiNiO₂ and LiCoO₂ undergo first-order phase transformations during Li cycling, as evidenced by distinct voltage plateaus in the GV profile and through *operando* x-ray diffraction (XRD) studies.^{33,34} However, the inclusion of both cations and Al³⁺ results in solid-solution Li intercalation behavior, and an increase in the diffusion coefficient.³⁵ Another example of disorder suppressing intercalation driven phase transitions and enabling faster Li diffusion can be found when MoO₃ is reduced to pseudocapacitive MoO_{3-x} by including oxygen vacancies.³⁶ Unfortunately, while specific examples are available in the literature, a systematic understanding of how disorder leads to pseudocapacitive charge storage is lacking. Additionally, the interaction of disorder with size remains poorly understood. Therefore, in this work, we aim to elucidate the intertwined roles of size and disorder in enabling pseudocapacitive charge storage.

Molybdenum disulfide (MoS₂) is a layered van der Waals (vdW) material that has demonstrated success as a Li⁺ intercalation material due to its tunable vdW gap size. Many studies focus on its four-electron conversion reaction reducing MoS₂ to Mo metal and Li₂S by cycling down to 0.0 V vs Li/Li⁺.³⁷⁻³⁹ Although this reaction provides a high gravimetric capacity, it results in large structural distortions and poor reversibility. Therefore, we focus on the highly reversible one-electron intercalation reaction occurring between 1.0 – 2.7 V with a theoretical capacity of 167 mAh



g⁻¹ (Equation 3).⁴⁰

MoS₂ has been synthesized in a variety of architectures such as exfoliated graphene-like sheets,^{38,41-44} nanoparticles,^{12,45,46} nanorods,^{47,48} thin films,⁴⁹ and nanoflowers^{50,51} which have shown improved Li⁺ insertion performance compared to bulk MoS₂.⁵² This faster and more reversible Li⁺ intercalation in MoS₂ nanostructures has been attributed to the higher surface area, shortened diffusion length, and expanded vdW gap size, enabling faster ion diffusion. However, it has been difficult to resolve to what extent pseudocapacitive charge storage in nanostructured MoS₂ is caused by the reduced crystal size as opposed to lattice disorder because nano-MoS₂ always tends to be at least partly disordered. The disorder may take the form of stacking faults, expanded vdW layer spacing, vacancies, strain, and more.⁵³

We note that as synthesized MoS₂ generally exists in the 2H structure, where the molybdenum atom sit in a trigonal prismatic coordination environment with the six neighboring

sulfur atoms.^{49,54} Upon intercalation of Li^+ during the first few cycles, an irreversible phase transition from the 2H to the 1T phase occurs where the sulfur planes glide and the molybdenum atom is now in an octahedral coordination environment.⁵⁵⁻⁵⁷ Li^+ insertion is also accompanied by reduction of Mo(IV) to Mo(III), which changes the band structure from the semiconducting 2H to metallic 1T phase.^{58,59} Therefore, it is important to complete transformation of all the material to the 1T phase before rate cycling and to differentiate the 2H to 1T phase transition (evidenced by a voltage plateau at ~ 1.1 V vs Li/Li^+) from the reversible Li intercalation reaction that will be discussed throughout this paper.

In this paper, we have synthesized a set of nanostructured MoS_2 samples with controlled size and disorder to deconvolute the contribution of both these effects in enabling pseudocapacitive charge transfer. We demonstrate that both reducing the crystal size and introducing lattice disorder can cause suppression of Li-intercalation induced phase transitions and synergistically enhance kinetic performance. The effects are also additive. Overall, this work suggests that either nanoscale size or crystal disorder can lead to pseudocapacitive properties, but the mechanism by which they do so may vary significantly.

2. Experimental

Materials: Ammonium molybdate (para) tetrahydrate $(\text{NH}_4)_6\text{Mo}_7\text{O}_{24}\cdot 4\text{H}_2\text{O}$ (99%, Alfa Aesar), ammonium persulfate (APS) (98%, Alfa Aesar), ammonium lauryl sulfate (ALS) ($\sim 30\%$ in H_2O , Sigma Aldrich), methyl methacrylate (MMA) (contains ≤ 30 ppm MEHQ as inhibitor, 99%, Sigma Aldrich). Bulk MoS_2 was purchased from Beantown Chemical and stored inside an Ar glovebox. H_2S for sulfurization was purchased as a mixture of H_2 (95%)/ H_2S (5%) from Airgas.

2.1 Synthesis of poly(methyl methacrylate) (PMMA) colloids: PMMA colloids 60 – 80 nm in diameter were used as organic template to create a porous structure in the MoO_2 precursor. The synthesis is adapted from Wang *et al.*⁶⁰ A three-neck flask fitted with a condenser and septum was loaded with 165 mL of milliQ water, 0.3 mL of ALS solution, and 0.075 g of APS. The solution was bubbled under N_2 for 20 – 30 mins while stirring to remove O_2 and prevent premature polymerization. Then, the three-neck flask with MMA was heated in an oil bath to 65°C , and 12.55 mL MMA was injected. After, the reaction was stirred and heated at $70 - 75^\circ\text{C}$ for 1 hour. The final

colloid solution was purified by liquid-liquid extraction in a separatory funnel with hexanes to remove any unreacted precursors. Size of the colloids was confirmed by scanning electron microscopy. Mass density of the colloid solution was measured using thermogravimetric analysis (TGA).

2.2.a Synthesis of mesoporous MoO₂ precursor: Mesoporous MoO₂ was used as the precursor for the small disordered (sd) and small crystalline (sc) samples. In a typical synthesis, 200 mg ammonium molybdate tetrahydrate was dissolved in the PMMA solution (200 mg total PMMA, determined based on the density of PMMA in the solution). The precursor solution was frozen by adding dropwise to liquid nitrogen. Once frozen, the solution was lyophilized for at least 12 hours to obtain a dried white powder. The dried powder was calcined under Ar at 675°C for 1 hour to burn out polymer templates and crystallize the porous MoO₂. The MoO₂ product was a black powder.

2.2.b Synthesis of α -MoO₃ nanoparticle precursor: Nanoparticle MoO₃ was used as the precursor for the large disordered (LD) and large crystalline (LC) samples. The method is adapted from Nagabhushana *et al.*⁶¹ Approximately 3 g (2.5 mmol) of ammonium molybdate tetrahydrate was dissolved in de-ionized water and stirred for 30 mins at RT. 5 mL of 2 M nitric acid was added to reach pH \sim 1, causing the remaining precursor to complete dissolution and the solution to clear up. Then the solution was heated at low heat (\sim 60°) for 1 hour. The h-MoO₃ product, a white powder, was washed with milliQ water and centrifuged for 10 mins at 4000 rpm. The h-MoO₃ was heated to 450°C in a muffle furnace and soaked at 450°C for 6 hours to produce α -MoO₃, a white powder with a grey tint.

2.3 Sulfurization of mesoporous MoO₂/MoO₃ to MoS₂: Approximately 50 mg of mesoporous MoO₂ or nanoparticle MoO₃ was ground with mortar and pestle to expose more surface area to flowing gas. The powder was loaded into a graphite boat and placed in a tube furnace. The furnace atmosphere was purged with Ar for 30 mins to remove O₂. Then the atmosphere was changed to a mixture of H₂ (95%) /H₂S (5%). The oven was ramped to 700°C in 1 hour and soaked for 12 hours to produce the disordered samples (Figure 1a and 1b). The crystalline samples (Figure 1c and 1d) were

annealed at 900°C and soaked for 12 hours. Once the furnace cooled down, the atmosphere was flushed again with Ar for 30 mins to remove any traces of H₂S. The MoS₂ product was a gray powder.

2.4 Raw material characterization: Scanning electron microscopy (SEM) images were obtained using a JEOL model 6700F electron microscope. Transmission electron microscopy (TEM) was performed using a FEI Technai G² T20 high-resolution EM, CryoEM, and CryoET operating at an accelerating voltage of 200 kV. X-ray diffraction (XRD) patterns were collected with a PANalytical X'Pert Pro diffractometer operating with Cu K α ($\lambda = 1.5418 \text{ \AA}$) using a 0.05° step size, an accelerating voltage of 45 kV, and a current of 40 mA. XRD patterns were collected from 10 – 80°. Nitrogen porosimetry was carried out using a Micromeritics TriStar II 3020 porosimeter.

2.5 Total scattering (TS) / pair distribution function (PDF) analysis: Powder samples of MoS₂ were submitted to the mail-in program at the Advanced Photon Source (APS) Beamline 11-ID-B for ambient measurements. Powders were loaded into 1.1 mm Kapton capillaries, which were sealed with epoxy on both ends. X-ray energy of 58.6 keV ($\lambda = 0.2115 \text{ \AA}$) was used. CeO₂ was used as a calibration standard. 2D data calibration, integration, and Fourier transform to obtain PDF G(r) was done in GSAS-II.⁶² PDFgui was used to simulate reference phase PDF patterns and refine structural parameters of experimental PDF data from 1 to 12 \AA .⁶³ Crystal structures for the 2H and 3R MoS₂ (Schonfeld, COD ID: 9007660) were obtained from Crystallography Open Database.^{64,65} Crystal structure for 1T-MoS₂ was obtained from Materials Project Database.⁶⁶ An expanded layer model was constructed by expanding the van der Waals gap of the 2H phase by 20%. Although we recognize this model is likely not an energetic minimum, it is sufficient for modelling the changes in scattering intensity as layers of MoS₂ are no longer correlated. Values of $Q_{\text{damp}} = 0.038$ and $Q_{\text{broad}} = 0.02$ were used to correct for instrument broadening.

2.6 Electrode fabrication and electrochemical cycling: Slurry electrodes were composed of 70% active material, 10% carbon black, 10% carbon nanofibers, and 10% polyacrylic acid (PAA) as the binder. Dry powders were first ground up in a mortar and pestle several times. PAA was added as a 3% by mass solution in benzyl alcohol. The wet mixture was ground up several more times until it became a viscous paste. Slurries were cast using a doctor blade onto carbon-coated aluminum foil with $\sim 1 \text{ mg/cm}^2$ mass loading and dried overnight in a vacuum oven at 140°C to remove residual solvent. Electrode discs with area of 0.71 cm² were punched out and assembled inside an Ar-filled

glovebox into 2032 coin cells with 2 stainless steel spacers, a stainless steel spring, and a glass fiber separator. Polished Li foil was used as the counter and reference electrode. Commercial grade 1 M LiPF₆ in 1:1 ethylene carbonate (EC):dimethylene carbonate (DMC) was purchased from Sigma-Aldrich and used as the electrolyte. Before any electrochemical characterization, all samples were first pre-conditioned by galvanostatic cycling (GV) at 1C ten times to completely transform 2H-MoS₂ to 1T-MoS₂ for good conductivity (Figure S1). After this precycling process, electrochemical impedance spectroscopy (EIS) was conducted between 900 kHz and 100 mHz using a 10 mV input at 1.0 V vs. Li/Li⁺. All MoS₂ samples showed relatively low charge transfer resistance similar or lower than other examples in the literature, with only minor sample-to-sample differences due to electrode variability (Figure S2).^{12,67}

Galvanostatic cycling between 1.0 – 2.7 V (vs. Li/Li⁺) was then performed at multiple C-rates (1C, 5C, 10C, 20C, 40C, 60C, 80C, 100C), with the 1C rate defined by the theoretical capacity for Li⁺ insertion of 167 mAh/g. Cyclic voltammetry (CV) data was collected between 1.0 – 3.0 V (vs Li/Li⁺) at multiple scan rates (0.1, 0.2, 0.3, 0.4, 0.5, 1.0 mV/s) to perform kinetic analyses. To estimate diffusion coefficient as a function of state of charge (SOC), galvanostatic intermittent titration technique (GITT) was performed. For the GITT experiment, cells were first de-lithiated to 2.7 V at a C/2 rate, then a C/10 current pulse was applied for 30 mins followed by a 2 hr rest period (no current applied). The pulse-rest-pulse-rest sequence was repeated until the cell reached 1.0 V. While the potential window used here for MoS₂ makes it generally more suitable for use as an anode, for testing purposes MoS₂ electrodes were studied in a half cell configuration versus a Li metal anode.

2.7 Operando XRD: *Operando* diffraction experiments were conducted at the Advanced Photon Source (APS) and the Stanford Synchrotron Radiation Lightsource (SSRL). Experiments were carried out using pouch cells made with aluminized mylar, Ni and Al leads, and glass fiber separators. 1M LiPF₆ in 1:1 EC:DMC was used as electrolyte. Li metal was used as counter and reference electrode. Pouch cells were pressurized using beryllium windows during operation. Figures S14 and S15 compare data from pouch cells and modified coin cells to demonstrate the influence of *operando* cell design. For the modified coin cells there, the outer casing for positive and negative electrodes were machined with a 1/8 hole in center, taped over with Kapton, while the two 0.5 mm spacers inside the cell were machined with 3/16 holes in center. The X-ray energy at SSRL beamline 11-3 was 12.7 keV ($\lambda = 0.9763$ Å). Collection times for each diffraction pattern at SSRL ranged from 30 – 60 seconds. X-ray energy at APS beamline 17-BM is 51.5 keV ($\lambda = 0.24075$ Å). Collection times for each diffraction pattern at APS ranged from 3 – 10 seconds. All cells were cycled at 1C unless otherwise

noted. LaB_6 placed at the same sample-to-detector distance as the electrodes was used as calibration standard. Data integration and reduction was performed using GSAS-II.⁶³ Peak fitting was performed in Igor.

2.8 Statistical Analysis: Data were processed with standard protocols as specified in the respective sections of the experimental. In summary, PDF data was calibrated, integrated, and Fourier transformed in GSAS-II software and refined to simulated reference patterns with PDFgui software. Electrochemical data were normalized by mass of active material for specific capacities, or normalized to the capacity at 1C rate when specified. Operando XRD data was calibrated, integrated, and reduced in GSAS-II software, with peak fitting for structural analysis performed in Igor.

For all figures, data shown is from non-averaged, representative samples with statistical uncertainty specified in the figure caption as necessary. For PDF fitting, scale factor refinements have uncertainties of $\pm 5\%$ based on unavoidable error with multi-phase refinement. PDF was run separately on 2 - 5 syntheses of each type of MoS_2 to ensure a representative sample was fit. Electrochemical performance is representative of at least three cells within 5% deviation, while capacity values shown have uncertainty of 2% based on statistical error in determination of active mass. Linear fit b values shown in Figure 5 have errors of approximately ± 0.05 or lower based on the quality of fits, which are shown explicitly in Figure S12.

3. Results and Discussion

3.1. Material Characterization

A set of four representative samples of MoS_2 were synthesized and compared to deconvolute the effects of size and disorder. The small disordered (sd) and small crystalline (sc) samples were synthesized using gas-phase sulfurization of crystalline mesoporous MoO_2 . Compared to direct crystallization, this method allows for improved retention of nanoscale architecture and introduction of crystal disorder in the resulting MoS_2 .^{47,68} The large disordered (LD) and large crystalline (LC) samples were produced through the same gas-phase sulfurization process, but starting with MoO_3 nanoparticles.

SEM images of the small disordered (Figure 1a) and small crystalline (Figure 1c) samples show a porous structure well-preserved from the mesoporous MoO₂ precursor (Figure S3) with pore wall thicknesses around 20 - 40 nm. Large disordered (Figure 1b) and large crystalline (Figure 1d) samples show particle sizes 200 – 400 nm in diameter. X-ray diffraction (XRD) patterns of the as synthesized mesoporous MoS₂ (Figure 1e) match JCPDS reference 2-0132 for MoS₂. No remaining MoO₂ or MoO₃ impurities were observed in the XRD, demonstrating the reaction went to completion. There is significant peak broadening and overlap, such that only the (002) peak at 14.4° is well-resolved. By fitting the (002) peak to a Voigt function and using the full width at half max (FWHM) in the Scherrer equation, an average particle size for sd-MoS₂ and LD-MoS₂ was estimated to be ~ 5 nm.

The observed size in SEM is much larger than the size predicted by the Scherrer equation, suggesting that the diffraction broadening is dominated by lattice disorder effects, rather than size effects alone. Because size and disorder both contribute to peak broadening in the XRD, the calculated “size” from the Scherrer equation is more suitably called a “crystalline coherence length.” The lattice disorder can also be directly observed in the high-resolution transmission electron microscopy (HR-TEM) images of LD MoS₂ (Figure 1f,g). Most regions of the material show small lattice domains with different orientations within a single particle, although some parts do show larger, but still relatively small, lattice domains. The large amount of lattice disorder in these samples is typical of many MoS₂ nanomaterials.^{12,38,41-51} Still, since the large samples also show considerable peak broadening, it is likely that disorder is introduced during the sulfurization process. The conversion of the existing crystal domains of MoO₂ or MoO₃ to MoS₂ can result in a strained, disordered lattice, even when the physical particle size remains large. In contrast, the XRD pattern of commercial bulk MoS₂ (Figure S4) shows very narrow and well-resolved peaks.

By increasing the sulfurization temperature from 700°C (small and large disordered) to 900°C (small and large crystalline), the diffraction peaks sharpen while the physical crystal size according to SEM looks nearly the same (Figure 1a-d). A detailed analysis of the wall thickness distribution for the small disorder and crystalline materials further confirms their similar physical size (Figure S5). XRD, in contrast, shows how the large and small crystalline and large and small disordered materials are similar. In the region near 60°, the two peaks corresponding to (110) and (008) planes are broadened into one peak in the disordered (Fig 1e, top) samples, while in the crystalline samples (Fig 1e, bottom), the peaks are well resolved. Similarly, in the 70 – 80° region, there are three peaks distinguishable in the crystalline samples, but they are broadened into one feature in the disordered

samples. Because the physical particle size looks nearly the same between sd/sc and LD/LC, we attribute the diffraction peak sharpening to increasing order in the lattice as the annealing temperature is increased, rather than particle growth. Because “disorder” is a property which is often ambiguously defined, we use this diffraction sharpening criterion to distinguish between “disordered” and “crystalline” samples, although all samples contain some degree of lattice disorder in comparison to bulk material.

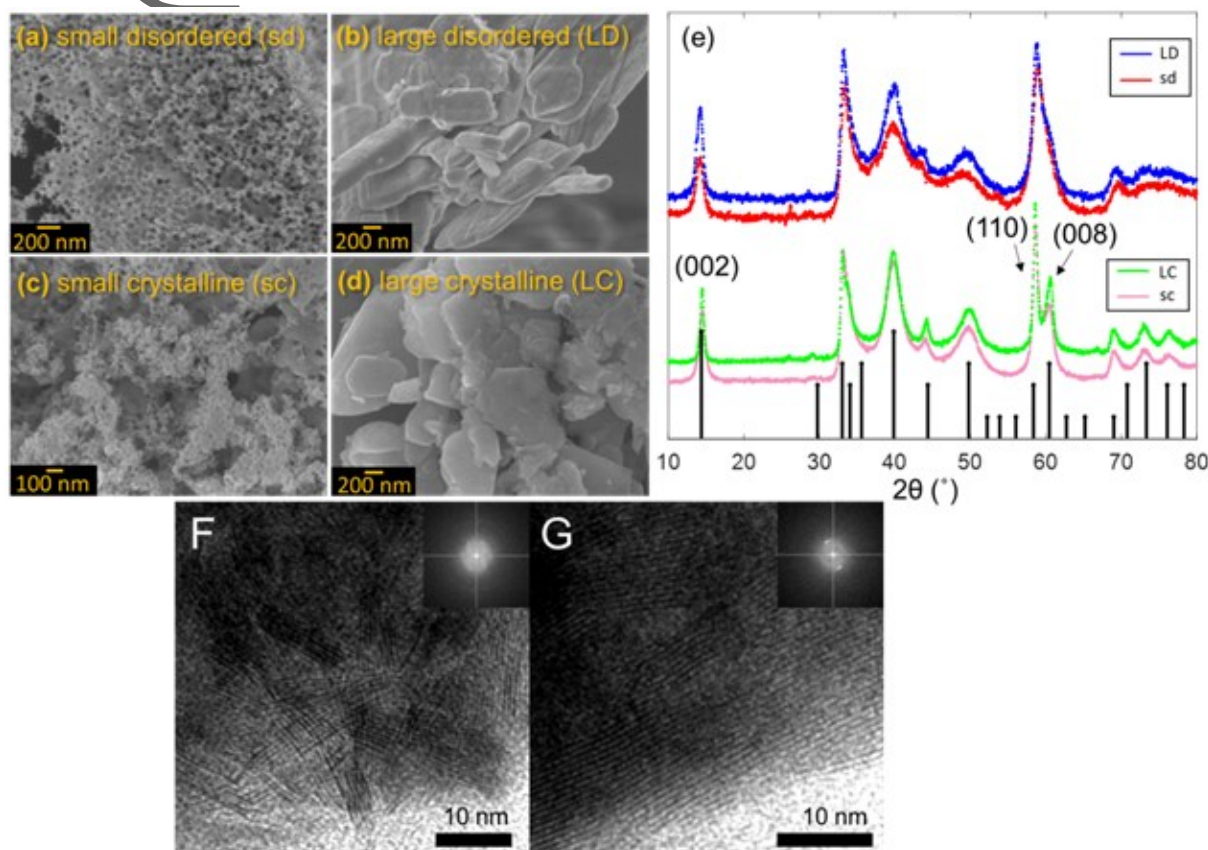


Figure 1. SEM images of a) small disordered (sd) MoS₂, b) large disordered (LD) MoS₂, c) small crystalline (sc) MoS₂, and d) large crystalline (LC) MoS₂. Panel e) shows that the XRD patterns for sd-MoS₂ (red) and LD-MoS₂ (blue) display significant peak broadening and disorder while sc-MoS₂ (pink) and LC-MoS₂ (green) show more well-resolved diffraction peaks, especially at 60° and 70-80°. Black reference pattern is JCPDS 2-0132 for MoS₂. (F) High resolution transmission electron micrographs (HR-TEM) of LD-MoS₂ showing a disordered region with small grains oriented in different directions. (G) HR-TEM showing a more ordered region of LD-MoS₂ with several coherent crystal domains extending across tens of nanometers. Insets show Fourier transforms of the micrographs.

To further verify that the size of the small mesoporous samples could be controlled independently of disorder, surface area measurements on sc-MoS₂ and sd-MoS₂ were performed and were found to be 12.2 and 15.0 m² g⁻¹, respectively (Figure 2a,b). Their porosities were calculated to be 22% for sc-MoS₂ and 16% for sd-MoS₂, demonstrating a mesoporous network for ionic conductivity and electrolyte penetration. While the surface area and porosity between sc-MoS₂ and sd-MoS₂ samples is very similar, the small crystalline shows a higher average pore diameter (13.8 nm compared to 9.2 nm) and a broader size distribution of pores (Figure 2c,d). Surface area and porosity for the MoS₂ products is lower than that of the mesoporous MoO₂ precursor and pore size is slightly larger (Figure S6), indicating that some rearrangement must occur during the sulfurization process. The unit cell of MoS₂ is larger than that of MoO₂, so as the oxide converts to the sulfide, overall porosity is expected to decrease. During the annealing process, the porous network may also restructure to reduce high-energy pore necks. Presumably, a hotter annealing temperature allows for more rearrangement, explaining why the pore diameter distribution is broader for the small crystalline MoS₂ than the small disordered.

Because the large crystalline and large disordered samples have grain and pore sizes on the order of hundreds of nanometers, their surface area is outside the limit of detection for most porosimetry systems, but it can be assumed to be low. However, as the surface area and porosity are not significantly different between the small disordered and small crystalline samples, it is clear that increasing the calcination temperature from 700°C to 900°C does not have a significant effect on the grain size of the product, even though it does dramatically change the lattice disorder. As a result, the surface areas for the large crystalline and large disordered materials are expected to be effectively the same. We have thus demonstrated that we can synthetically control the degree of lattice disorder by simply increasing the annealing the temperature, and we can independently control particle size by increasing the size of the MoO₂ or MoO₃ precursor.

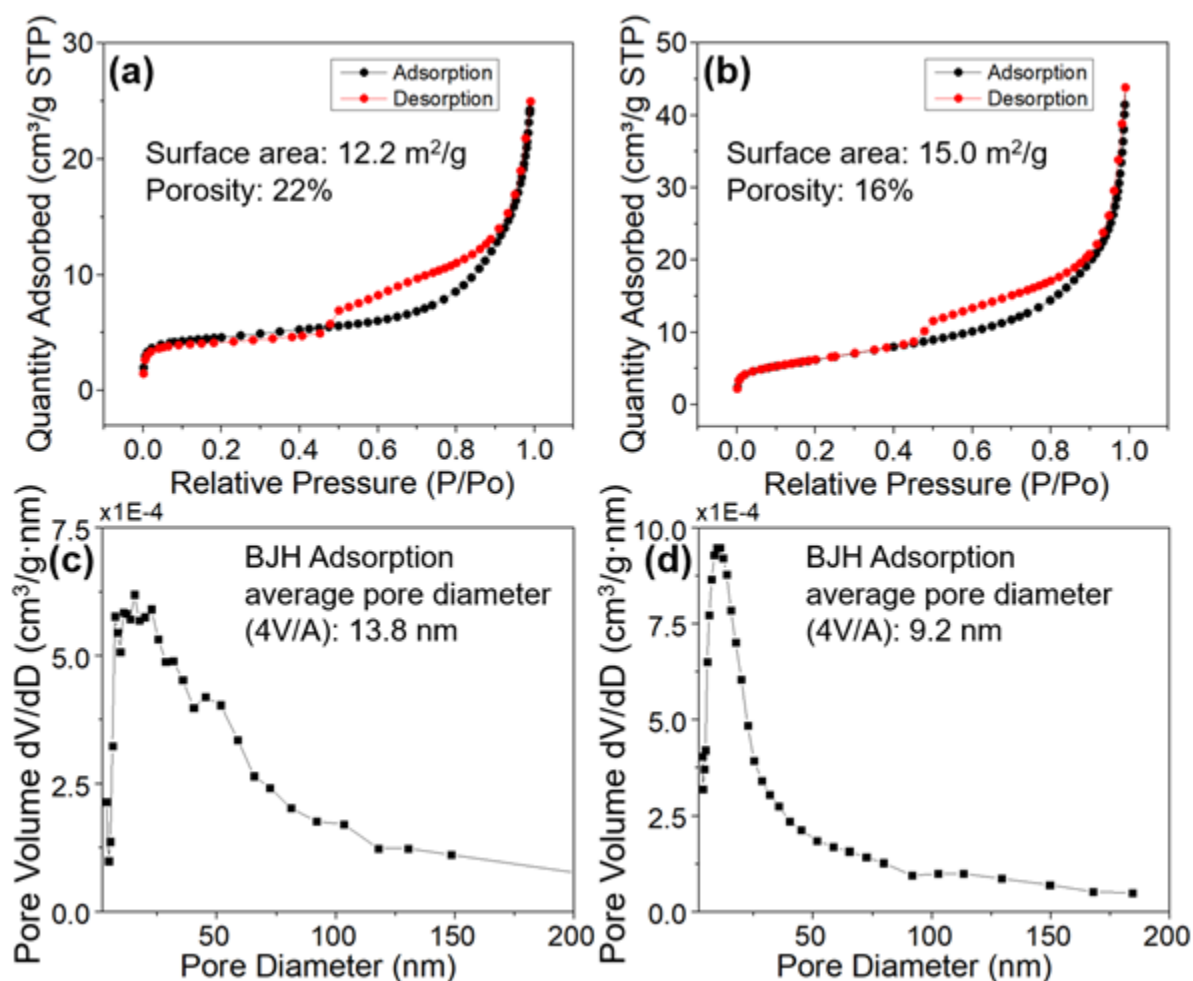


Figure 2. Nitrogen porosimetry adsorption/desorption isotherms for (a) sc-MoS₂ and (b) sd-MoS₂. Adsorption BJH pore size distributions for (c) sc-MoS₂, and (d) sd-MoS₂.

To elucidate the nature of the disorder present in our nanostructured MoS₂, we collected total x-ray scattering at APS BL 11-ID-B. The total scattering technique collects both Bragg and diffuse scattering from the sample.⁶⁹⁻⁷¹ By taking the Fourier transform of the total scattering, the atomic pair distribution function (PDF) is calculated, which gives all atom-atom correlations within the material, regardless of long-range order. Therefore, the PDF enables us to characterize structural information (atom-atom distances) about amorphous or disordered regions in the material and give insight to short-range order.

The first two peaks in the PDF at 2.41 Å and 3.16 Å (Figure 3a) correspond to the nearest Mo-S bond within one trigonal prism and the Mo-Mo/S-S correlations within one layer in the neighbouring unit cell, respectively.⁶⁵ Peaks below 5 Å can be assigned to distinguishable bond

This article is protected by copyright. All rights reserved.

distances within the MoS₂ unit cell by observation, but above 5 Å, the PDF peaks no longer correspond to unique bonds, as they contain contributions from multiple atom-atom distances within a periodic system. However, the presence of higher-*r* peaks indicates the extent of long-range order. By simulating the PDF from crystal structures of MoS₂, higher-*r* peaks can also be decomposed into contributions from Mo-Mo, Mo-S, or S-S correlations (Figure S7). We note that the sulfur contribution to the total PDF is significantly less than that of molybdenum, since x-ray scattering power is proportional to atomic number. Therefore, sulfur atom positions in the sample that deviate from the ideal crystal structure should result in a modulation of PDF peak intensity, rather than appearance of new PDF peaks.

The bulk MoS₂ shows strong correlations going out to 7 nm and higher (Figure S8), as expected for a fully crystalline material. As *r* increases, all of the nanostructured samples display a steeper decrease in intensity of the *G*(*r*) than the bulk, with the disordered samples showing a greater decay in intensity than the crystalline samples (Figure S9), indicating, unsurprisingly, that there is less long-range ordering in the more disordered samples. Due to this decline, all fits described in this section were conducted over a range of 1 - 12 Å, where there is still enough local ordering (indicated by the sharpness of the peaks) to meaningfully refine the data. For all samples, the PDF up to 5 Å is nearly identical, indicating that all have the same local ordering within one unit cell and that the Mo-S bond lengths and intralayer Mo-Mo distances are the same in each sample. However, differences begin to appear at ~5.5 Å. Notably, the peaks at 5.5 Å, 7.2 Å, and 7.88 Å, show a systematic decline in intensity as both size and order decrease.

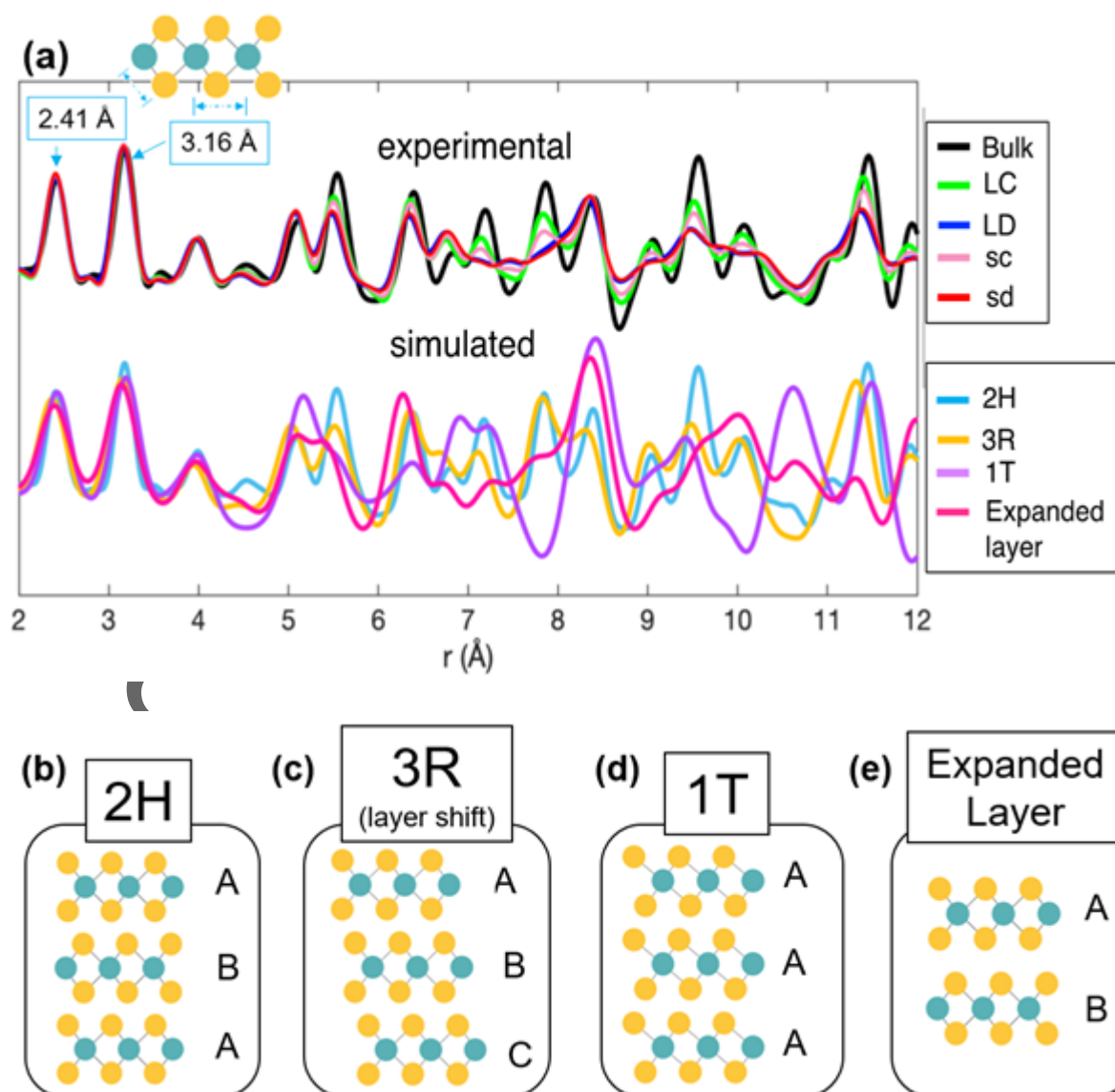


Figure 3. Crystal structure models used to simulate PDF. (a) Experimental PDF for bulk, large crystalline, large disordered, small crystalline, and small disordered MoS₂ overlaid with simulated PDF patterns. PDF was run separately on 2 - 5 syntheses of each type of MoS₂ to ensure that representative sample were presented here. (b) standard 2H MoS₂ with A-B-A layer stacking. (c) 3R MoS₂ polymorph with A-B-C layer stacking, used to simulate the effect of stacking faults and layer shifting. (d) 1T MoS₂, used to simulate disorder within the S-Mo-S layers (e) Expanded layer model derived from the 2H structure with an expanded vdW gap.

To determine what types of lattice disorder affect specific correlations, reference PDF patterns were simulated for the standard 2H MoS₂ crystal structure (Figure 3b), the 3R polymorph

(Figure 3c), the 1T metallic phase (Figure 3d), and a version of the 2H phase with vdW layer expanded (Figure 3e). 3R-MoS₂ is another naturally occurring polymorph that is less common than 2H and has a rhombohedral unit cell with Mo atoms in a trigonal prismatic coordination environment.^{64,72,73} The unit cell of 2H-MoS₂ contains two S-Mo-S layers oriented anti-parallel to each other (illustrated by the direction of the S-Mo-S triangles in the cartoon in Fig 3b-d) in an A-B-A-B stacking pattern. In contrast, 3R-MoS₂ has three distinct S-Mo-S layers oriented parallel to one another, with the third layer is offset so that 3R has an A-B-C stacking pattern. Therefore, the 3R-MoS₂ crystal structure is used to simulate the effect of layer shifting disorder or stacking faults in PDF. The 1T phase of MoS₂ (Figure 3d) is a metallic phase related to the 2H phase by the shifting of the sulfur plane. 1T MoS₂ is generally unstable under ambient conditions and converts to the 2H phase; we use it here to simulate disorder within the S-Mo-S layers. Finally, the expanded layer model (Figure 3e) is derived from the 2H structure and used to simulate the effect of layer expansion disorder in the PDF. From the simulated patterns, it is evident that the decline in intensity at 5.5 Å can be caused by layer shifting and disorder within the layers (the expanded layer model also gives a decline in intensity, but shifts the peak position to a lower r that is not present in the experimental data), both layer shifting and layer expansion cause a decline in intensity at 7.2 Å, while the decline in intensity at 7.88 Å is may be due to either layer expansion or disorder within the layers. This suggests that layer shifting, layer expansion, and disorder within layers all exist in our nanostructured MoS₂ materials and contribute to faster Li⁺ ion diffusion.

To quantify the different types of disorder occurring in each sample, a multi-phase refinement using 2H, 3R, 1T, and expanded layer crystal structures was performed (Table 1). A comparison of the experimental and refined data can be found in the SI (Figure S10). These refinements estimate the different types of disordered phase present in these materials. We note that, due to the inherent uncertainty of fitting multiple phases to complex PDF data, the numbers should be taken as general ranges within $\pm 5\%$, rather than exact quantifications. As a control, PDF data for micron-scale bulk MoS₂ was refined both with the multi-phase fit including all structures, and with a single-phase 2H fit (Table S1). Adding additional phases to the bulk refinement did not improve the fit, and in some cases even worsened the fit, indicating that the bulk is effectively entirely the 2H phase and any disorder is only present in trace amounts. For the two crystalline samples, refining the 2H and 3R phases alone gives reasonable agreement with the experimental data (Table S2), although small amounts of the 1T and expanded layer phases do slightly improve the fits. By contrast, the refinements for the two disordered samples improve significantly when all four phases are included.

This article is protected by copyright. All rights reserved.

Based on the refinements, the crystalline samples contain significantly more of the 2H phase than the disordered samples (0.63 – 0.67 compared to 0.45 – 0.5). For all samples, the dominant form of disorder occurs as the layer-shifted 3R phase. All samples also contain smaller amounts of the expanded layer and 1T phases in roughly equal amounts, except for the large crystalline which does not show a significant amount of the 1T phase. Notably, however, even the large crystalline sample has significant layer shifting and layer expansion compared to bulk MoS₂. Additionally, the amount of overall disorder in the nanostructured samples is largely independent of size, and instead is primarily determined by the annealing temperature during synthesis. Compared to each other, the large/small crystalline materials contain similar fractions of the 2H phase, as do the large/small disordered samples. Comparing the crystalline and disordered nanostructured samples, the disordered materials show a larger fraction of layer expanded 2H and of disorder within the layers (1T); they also show decreased long-range ordering. In all samples, it is evident that the disorder largely takes the form of layer shifting or stacking faults. The higher annealing temperature for the more crystalline samples makes it possible for the lattice layers to move more freely in order to assemble into a structure that increasingly resembles the period 2H crystal lattice.

Table 1: Normalized Scale Factor Refinements for PDF of nanostructured MoS₂

Structure	2H	3R (layer shift)	Layer expansion	1T	R _w
Bulk	1.0				0.16
Large crystalline	0.67	0.17	0.11	0.04	0.16
Large disordered	0.45	0.26	0.14	0.15	0.17
Small crystalline	0.63	0.23	0.07	0.07	0.22
Small disordered	0.50	0.26	0.11	0.14	0.21

3.2 Electrochemical Characterization

The MoS₂ samples were assembled into composite slurry electrodes for electrochemical testing between 1.0 and 2.7 V vs. Li/Li⁺. The voltage range studied here for MoS₂ is similar to a

This article is protected by copyright. All rights reserved.

number of other moderate voltage anode materials, including $\text{Li}_4\text{Ti}_5\text{O}_{12}$ and TiNb_2O_7 , which are used commercially in fast-charging cells.⁷⁴⁻⁷⁷ It is widely accepted that graphite and other low voltage anodes cannot be used for high rate cycling in practical devices, since increased overpotentials lead to the risk of Li plating and device failure.^{78,79} Anodes with moderate voltage ranges (~ 1.0 to 1.5 V vs. Li/Li^+) result in lower energy density, but allow for fast-charging since there is little risk for Li plating.

Galvanostatic charge and discharge was performed at multiple C-rates on all samples (**Figure 4a**) to characterize the rate capability. Full galvanostatic charge and discharge traces at each C-rate can be found in the SI (Figure S11). Both the small samples (sd/sc) show the best rate performance at 100C (36 second charge) achieving 80 mAh g^{-1} , while the bulk MoS_2 has little to no capacity by 60C. It can be noted that several samples (sd, LC, sc) achieve higher than theoretical capacity for 1-electron intercalation (167 mAh g^{-1}) at 1C, likely due to the addition of surface redox sites. Most of this extra capacity occurs in the redox peak near 2.7 V. This relatively high voltage rules out unwanted sources of extra capacity like the conversion reaction, which only occurs at voltages below 1.0 V vs. Li/Li^+ , and suggest that the extra capacity is likely due to surface redox. To show a clearer representation of the percentage capacity retained at higher C-rates, we have normalized the rate capability to the experimental 1C capacity (Figure 4b). From the normalized rate capability, we can see that the small disordered MoS_2 shows the best performance in terms of greater fraction of 1C capacity retained at all current densities, except at 100C where it is equal to the small crystalline MoS_2 (39% of 1C capacity retained at 100C). The large disordered material performs almost as well, suggesting that both reduced crystal size and increased lattice disorder can shorten the ion diffusion length and improve fast-charging performance. Comparing normalized capacity across all samples at 80C, the large crystalline MoS_2 (green) shows the slowest rate performance (28% of 1C capacity), while the large disordered MoS_2 (blue) retains 37%. Therefore, simply introducing disorder into the lattice of large particles can speed up Li^+ intercalation significantly. We hypothesize this is because of the strong link between Li^+ diffusion rates and structural phase transitions, which will be discussed in detail below. Decreasing the material size can also shorten the diffusion length and speed up Li intercalation, demonstrated by the small crystalline MoS_2 (pink) retains 42% at 80C. Size appears to be a more significant effect for rate cycling, but both size and disorder can be leveraged to enhance the rate capability synergistically. Notably, the crystalline samples show higher capacities at slow rates than their disordered counterparts due. While disorder clearly benefits rate capability, it likely also makes some redox sites in the material inaccessible, leading to this slight variation in capacity at slow rates. Overall, small disordered MoS_2 (red) shows the best rate capability, with 45% of its 1C capacity retained at 80C. When combined with a hypothetical 4V cathode, the small disordered

This article is protected by copyright. All rights reserved.

MoS₂ cycled at 10C would deliver a gravimetric energy density of 300 Wh/kg with an average voltage of 2.3 V, along with a gravimetric power density of 3600 W/kg.

Long-term cycling was performed on the nanostructured materials at 10C to assess their capacity retention over time (**Figure 4c**). The small crystalline and small disordered samples both show excellent longevity, with 88% percent of their initial capacity remaining after 1000 cycles. The large disordered retains an intermediate 77% of its initial capacity, while the large crystalline performs the worst, retaining only 65% of its initial capacity after 1000 cycles. As with the rate cycling, changing size gives a greater improvement in long term performance than disorder, but both size and disorder can be used to independently improve the longevity of MoS₂. These effects are likely due to changes in the phase transition behavior of these materials during cycling, which we characterize later.

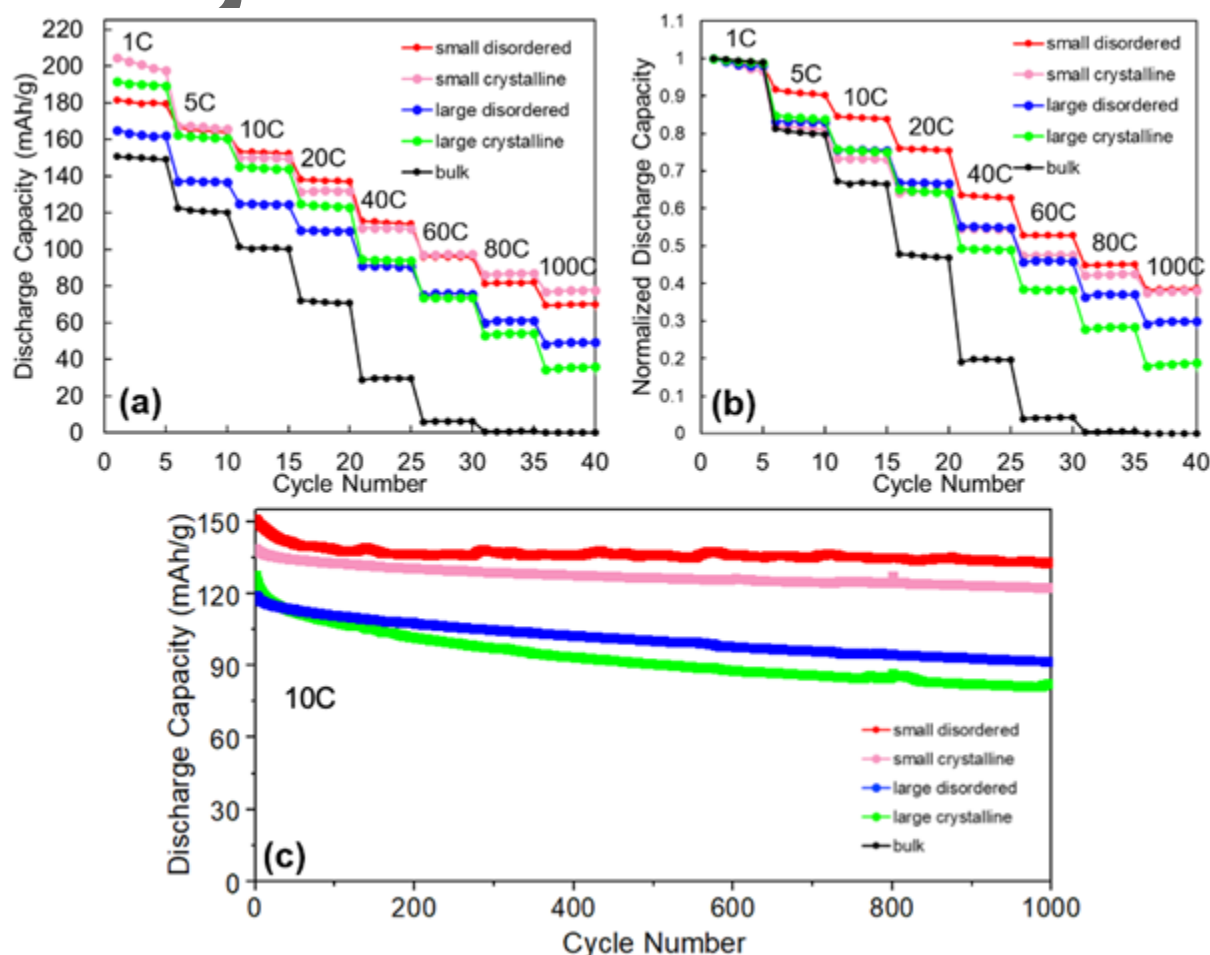
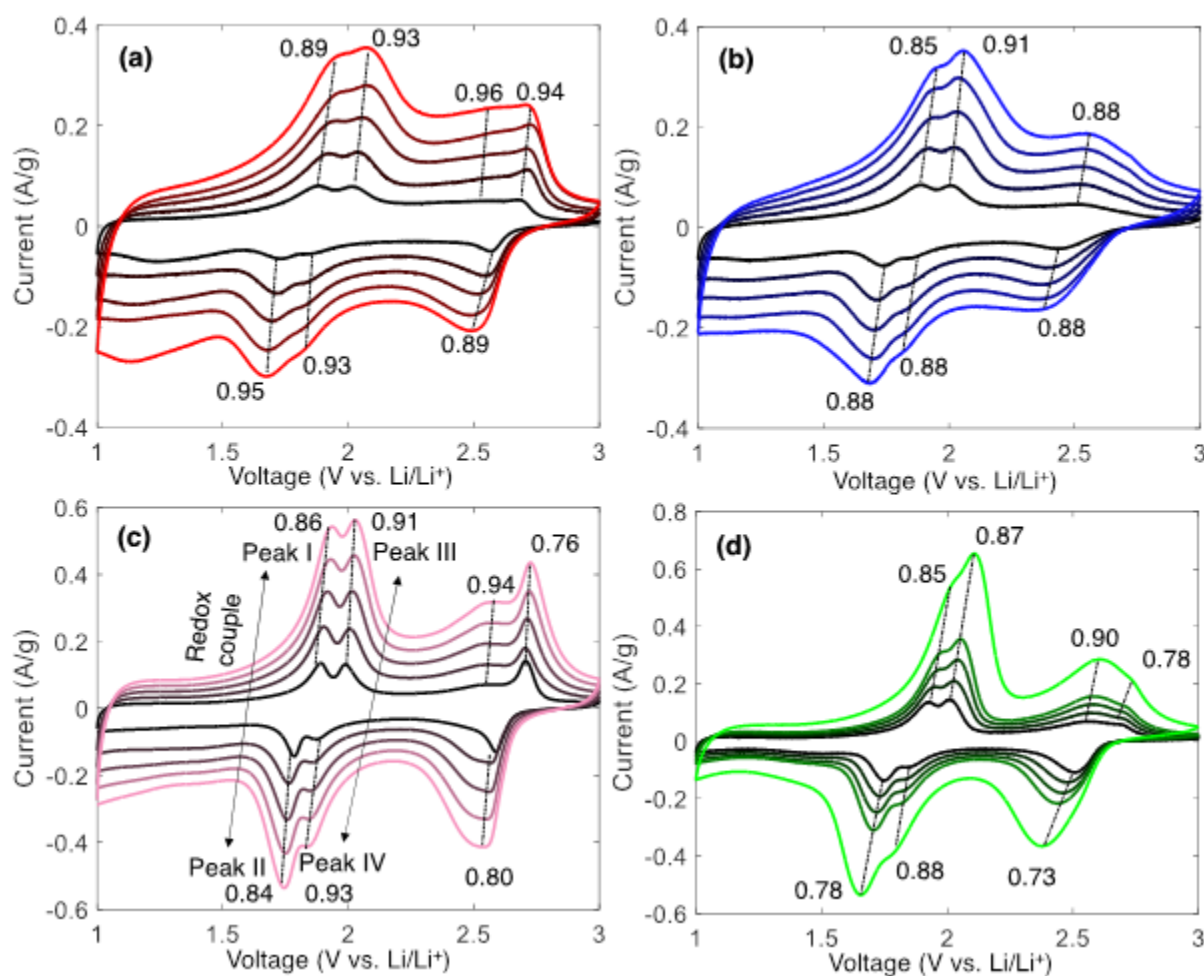


Figure 4. (a) Rate capability of bulk and nanostructured MoS₂ plotted as absolute discharge capacities. (b) Rate capability of bulk and nanostructured MoS₂ plotted as discharge capacities normalized to the 1C capacity to show percentage drop from 1C capacity. All nanostructured

This article is protected by copyright. All rights reserved.

materials show faster kinetics than the bulk material, and both size and disorder play a role in increasing discharge kinetics. (c) Long-term cycling of all nanostructured materials at 10C. The sc and sd materials show the best stability, followed by the LD, and then the LC materials. Electrochemical performance is representative of at least three cells within 5% error. Capacity values have uncertainty of 2% based on statistical error in determining active mass.

To deconvolute the fraction of charge storage coming from near-surface or “capacitive” processes versus diffusion-limited or “battery-like” processes, we employ several kinetic analyses. The first, termed the “b-value analysis”, is based on the Randles-Sevcik equation and standard capacitor sweep rate dependence,⁸⁰ and assumes that the current measured in a CV experiment follows the power law of $i = av^b$, where v is the scan rate and ‘a’ and ‘b’ are fitted parameters.⁸¹ By taking CVs at multiple scan rates and taking the current value at peak positions (voltages where redox events are happening), we can fit a line through of a plot of $\log(i)$ vs. $\log(v)$ to obtain ‘b’ as the slope.



This article is protected by copyright. All rights reserved.

Figure 5. CVs with peak b values of (a) small disordered, (b), large disordered, (c) small crystalline, and (d) large crystalline mesoporous MoS_2 samples. Peak I and peak II indicate a reversible redox couple. Peak III and peak IV indicate a redox pair couple. CVs for sd, LD, and sc were taken at 0.1, 0.2, 0.3, 0.4, and 0.5 mV/s sweep rate. CVs for LC were taken at 0.2, 0.3, 0.4, 0.5, and 1 mV/s. Linear fit slope values have errors within ≤ 0.05 .

Values of $b \sim 0.5$, as predicted by the Randles-Sevcik equation, indicate current limited by semi-infinite diffusion or “bulk battery-like” behavior. In contrast, when $b \sim 1.0$, the current varies linearly with the scan rate and is no longer limited by semi-infinite diffusion, indicating “capacitor-like” behavior. Details about the goodness of fit and linear regression can be found in the SI (Figure S12). For all samples, including the large crystalline sample (Figure 5d), the b -values are relatively high, but it is clear that by decreasing crystal size (Figure 5c), or by introducing lattice disorder (Figure 5b), the capacitive contribution to charge storage can be increased. Both size and disorder effects can be leveraged to further improve pseudocapacitive charge storage and enhance fast-charging performance (Figure 5a).

It is also interesting to note that by comparing both the sc/sd and LC/LD pairs, the shape of the CV is significantly altered. In both crystalline samples (**Figure 5c** and **5d**), the redox peaks near 1.8 V and 2.6 V are more well-defined than in their disordered counterparts (Figure 5a and 5b). Size effects are more subtle, but a careful comparison of the sc and LC samples shows broad peaks in the larger materials, presumably due to kinetic limitations in the larger grains (Figure S13). The CV suggests that introducing disorder into the lattice creates a broader distribution of redox sites, as the Li sites in a more disordered lattice will not be energetically equivalent. As disorder increases, the relative height of the current peak at 2.6 V compared to the 1.8 V peak appears to diminish, but the total charge stored in the same voltage window is the same or higher. This suggests that, in the disordered MoS_2 , the same amount of total charge is stored, but the thermodynamic potential of some redox sites has been lowered. Detailed CV peak positions across different samples can be found in the SI (Tables S3 – S6).

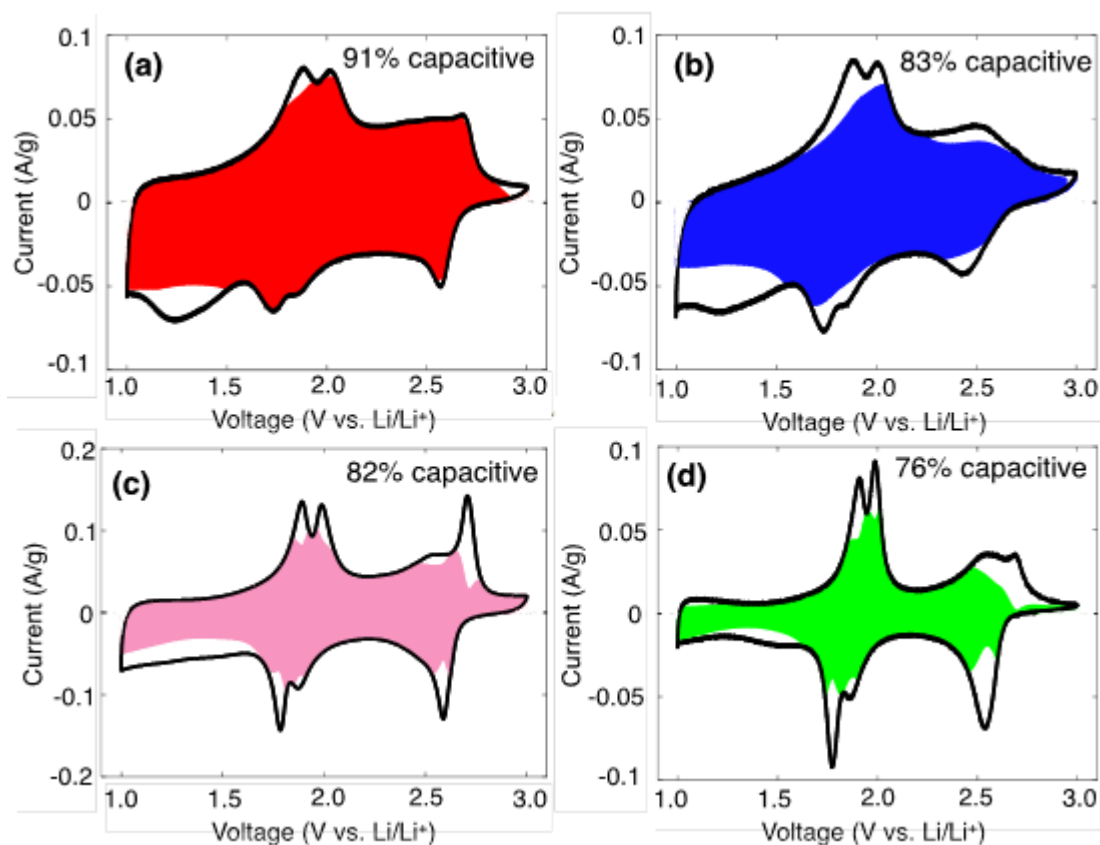


Figure 6. k_1 k_2 analysis of (a) small disordered, (b), large disordered, (c) small crystalline, and (d) large crystalline mesoporous MoS_2 samples, CVs taken at 0.1 mV/s.

Another kinetic analysis method is the “ k_1 k_2 analysis”, first introduced by Conway and coworkers to characterize capacitive charge storage in molybdenum nitride, which assumes that the current behavior depends on the sweep rate according to the following equation:⁸² $i = k_1 v + k_2 v^{1/2}$. This technique is another way of separating out the fraction of current originating from capacitive processes compared to diffusion-limited processes, but instead of allowing any scaling exponent, equation (3) assumes that all current must be purely diffusion controlled ($v^{1/2}$) or purely capacitive (v). In the analysis, after shifting the CV peak voltages at higher scan rates to account for polarization, a plot of $i v^{-1/2}$ vs $v^{1/2}$ can be fit to a line to obtain k_1 from the slope and k_2 from the intercept. By multiplying the k_1 value at each voltage point by $v^{1/2}$, we can obtain an estimated current corresponding to only the capacitive contribution to charge storage, shown by the colored shaded region of each CV in **Figure 6**. This analysis has been performed on the CVs taken at the slowest sweep rate, 0.1 mV/s because that allows for the most diffusion controlled charge storage to take place. By integrating the total current obtained from the “capacitive CV” and dividing it by the integrated total current from the entire CV, the percentage of capacitive charge storage is

This article is protected by copyright. All rights reserved.

calculated. At voltages where the redox peaks occur, there is less capacitive contribution to the charge storage due to diffusion limitations. We observe again that the large crystalline sample shows the lowest capacitive fraction at 76% (Figure 6d), while the small crystalline and large disordered show a similar increase in capacitive fraction to 82% and 83% (Figures 6b,c). Materials with both small size and high disorder (sd) show the highest capacitive fraction at 91% (Figure 6a).

To evaluate the role of disorder on electrode polarization as a function of state-of-charge, we performed GITT experiments, where the voltage change is monitored during multiple constant current pulses and subsequent rest periods.^{83,84,85} **Figure 7a** shows the voltage versus time graph for bulk and nanostructured MoS₂ during a GITT pulse-rest protocol. For each pulse step, the difference between the closed-circuit voltage at the end of the current pulse and the open-circuit voltage at the end of relaxation gives the reaction overpotential. This overpotential measures kinetic limitations under the quasi-equilibrium conditions of the GITT experiment. Here, we compared the overpotential for each sample to evaluate the effect of size and disorder on Li mobility during intercalation (Figure 7b). For each sample, the overpotential is low at the onset of Li intercalation, consistent with the fact that the Li gradient is largest in the beginning. As Li content increases, the overpotential increases in all samples, but to different extents. For bulk MoS₂, the overpotential remains low until $x \approx 0.45$, where it begins to increase from about 15 - 20 mV to over 200 mV. This result indicates that the diffusion of Li is dramatically hindered at high Li stoichiometry in the triclinic Li_xMoS₂ phase. However, these effects are mitigated by size and disorder. By contrast, all nanostructured materials reach considerably smaller overpotentials at high Li content ($x > 0.75$), with the large crystalline showing the second-highest overpotential next to the bulk at 123 mV, consistent with the fact that this sample shows the worst rate performance of the nanostructured materials. The large crystalline, large disordered, and small disordered do not show a significant rise in overpotential until they reach a higher Li content compared to the bulk ($x \approx 0.65$). Notably, the overpotential for the small disordered starts to rise shortly after the bulk at $x \approx 0.5$, but quickly plateaus and remains lower than that of the more crystalline samples. While some reduction in overpotential is expected for a nanoscale material (even a larger nanomaterial like those used here), the differences in overpotential between the large crystalline and both the large and small disordered materials suggests that disorder also improves the electrochemical kinetics in the high Li stoichiometry regime where the highest overpotentials occur.

We note that GITT is commonly analyzed with the derivation of relative diffusion coefficients. However, this analysis is subject to a number of well-known artifacts, including dramatic

underestimation of diffusion coefficients in regions with flat voltage profiles where first-order phase transformations occur.^{86,87} To avoid the errors associated with these artifacts, we do not report the derived diffusion coefficients here. The overpotential we discuss above, in contrast, is obtained from the data without any assumptions and provides similar insight without the same potential for error.

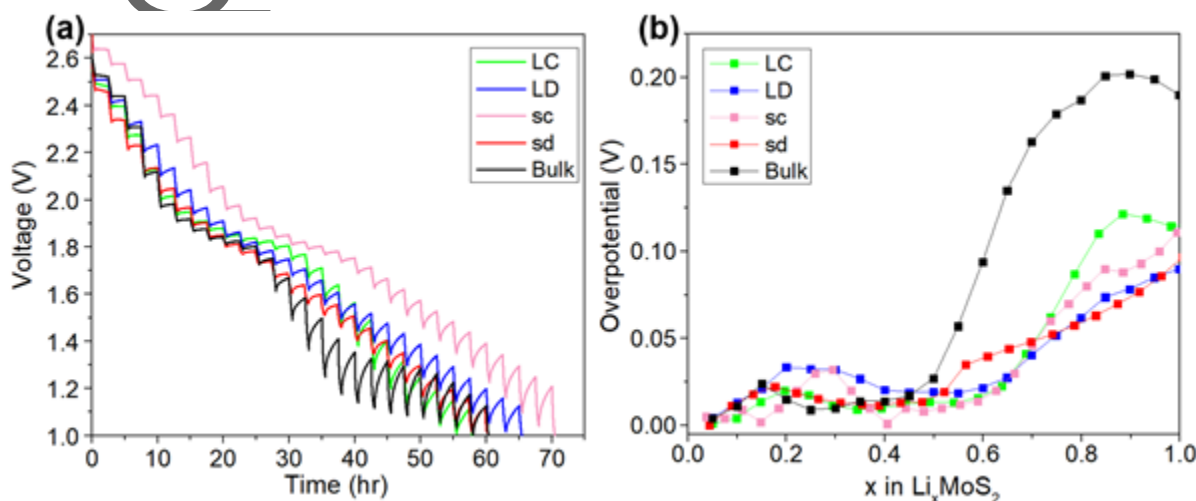


Figure 7. GITT of all samples, showing (a) voltage as a function of time during pulse-rest cycles, and (b) overpotential as a function of state of charge.

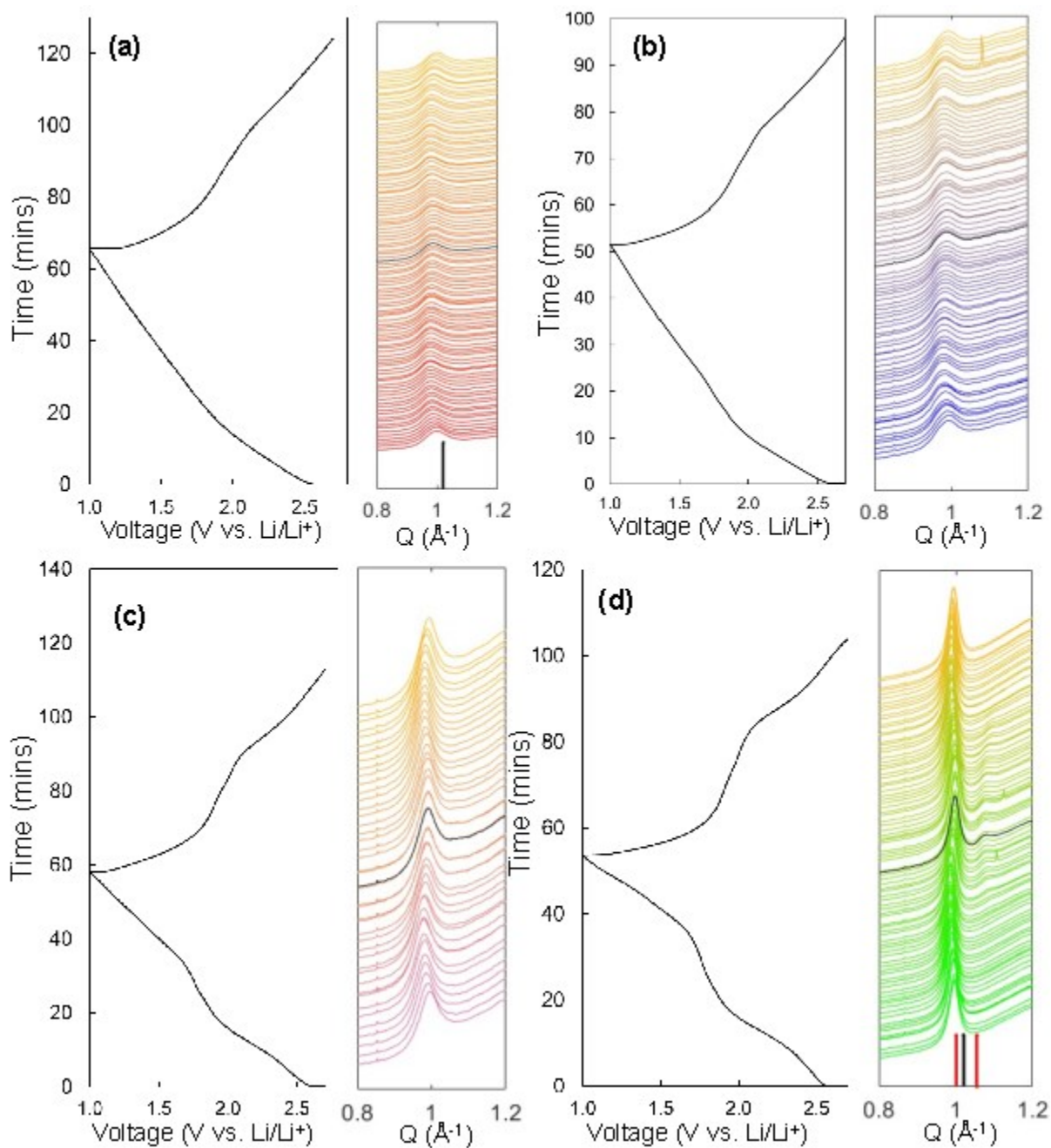
3.3 Operando XRD

To monitor the change in crystal structure during electrochemical cycling, *operando* X-ray diffraction was conducted on the samples. For clarity, only the time evolution of the (002) peak is plotted since the (002) peak is the most distinct and corresponds to the vdW gap and the Li^+ diffusion pathway. The full Q range spectra can be found in the SI (Figures S14-S16). None of the samples show degradation associated with conversion reactions, or the formation of Li_2S or Mo metal, confirming that only the intercalation reaction is taking place in this voltage window.^{52,88} Again, we observe that the small disordered (Figure 8a) and large disordered (Figure 8b) samples show significant diffraction peak broadening due to the lattice disorder, while the small crystalline (Figure 8c) and large crystalline (Figure 8d) show sharper (002) diffraction peaks. Only the large crystalline MoS_2 (Figure 8d) shows a distinct phase transition upon Li^+ intercalation, evidenced by the appearance of a new peak at $Q \sim 1.05 \text{ \AA}^{-1}$ corresponding to the triclinic Li_xMoS_2 phase, as observed in bulk MoS_2 . In contrast, all other samples (sd, sc, LD) show only a slight shift in the lattice spacing during both lithiation and de-lithiation and no symmetry breaking phase transition. Therefore, our

results indicate that both size and disorder effects can cause the suppression of intercalation-induced phase transitions.

By fitting the peak positions to Voigt functions, we have calculated the d-spacing throughout the *operando* experiment and observe that the (002) plane undergoes an initial expansion then contraction during both lithiation and de-lithiation (Figure 8e,f). The lattice “breathing” behavior is the result of a tradeoff between attractive interactions of Li^+ and S^{2-} causing lattice contraction, and repulsive interactions between nearby Li-Li pairs and volume change to accommodate ions causing lattice expansion.^{20,89} These different regimes of structural change can be assigned to the redox peaks seen for these samples. During lithiation, the first gradual decrease in lattice spacing from ~2.4 – 2.6 V corresponds to the first redox peak, whereas the second, and largest, region of redox peaks involves a transition from lattice contraction to expansion, along with the first-order phase transition for the large crystalline sample only. Importantly, the progression of structural change in the second region varies considerably between the disordered and crystalline samples. Whereas the lattice spacing of sd/LD samples shows a gradual, linear expansion from 1.0 – 1.8 V, the sc/LC samples show a more abrupt lattice expansion. Paired with the observation that the CVs of sd/LD samples are more similarly broadened (Figure 5a,b), while the CVs of sc/LC samples show more distinct redox peaks (Figure 5c,d), we suggest that size and disorder effects cause suppress phase transitions and enhance rate capability and cycle longevity through different mechanisms.

Author Manuscript



Auth

This article is protected by copyright. All rights reserved.

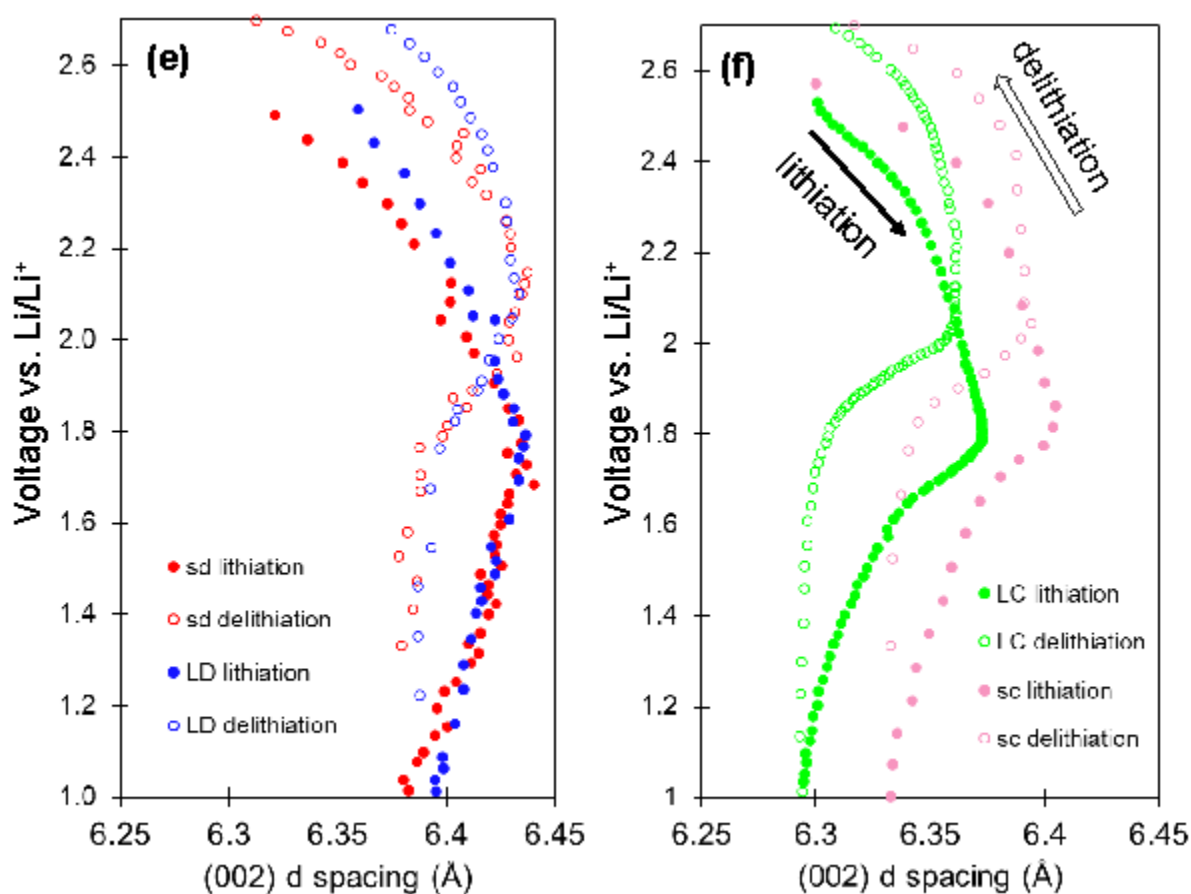


Figure 8. Operando XRD of (a) small disordered, (b) large disordered, (c) small crystalline, and (d) large crystalline MoS₂ samples cycled at 1C in pouch cells. Left panels shows the corresponding GV trace. (002) lattice spacing calculated from fitted peak positions for (e) small and large disordered samples, and (f) small and large crystalline samples. Black sticks in (a) and (d) show the reference pattern for 2H MoS₂. Red stick patterns in (d) show reference pattern for triclinic Li_xMoS₂.

We note that in addition to variation in the rate of peak shifting upon Li⁺ intercalation, there is also some variation in the absolute (002) peak position between samples with different sizes and degrees of disorder. Both of the disordered samples show the largest (002) d-spacings, and the peaks positions are very similar at all potentials other than the fully delithiated state. The lattice spacing in the LC sample (which showed a phase transition) is the smallest, but the difference is quite modest, particularly between LC and sc, contrary to what might be expected. This suggests that only a small lattice expansion is needed to suppress Li⁺ intercalation-induced phase transitions

and that at some critical vdW gap size (6.4 - 6.5 Å), the disorder plays the dominant role in facilitating faster Li⁺ diffusion.

4. Conclusions

We have synthesized a matrix of nanostructured MoS₂ materials through gas-phase sulfurization of oxide precursors with different crystal sizes and degrees of crystallinity to decouple the effects of both size and disorder on electrochemical performance and phase transition behavior. Pair distribution function (PDF) measurements and simulations confirm that both layer shifting, disorder within layers, and layer expansion disorder are present, although layer shifting is the dominant form of disorder. The lower annealing temperature used to produce the “disordered” samples results in a decrease in long-range ordering and less of the 2H phase compared to the more crystalline samples. Rate capability experiments show that both decreasing particle size and increasing disorder are effective ways to promote faster Li⁺ diffusion and 40% rate retention up to 100C. CV demonstrates that disorder creates a broader distribution of redox potentials. Both b-value and k₁-k₂ analyses reveal that size and disorder effects increase the fraction of non-diffusion-limited pseudocapacitive charge storage in the material. *Operando* XRD demonstrates that only the large crystalline MoS₂ undergoes a first-order phase transition from 1T-MoS₂ to the triclinic Li_xMoS₂ phase, while small disordered, small crystalline, and large disordered MoS₂ show gradual lattice expansion and contraction of the vdW gap without any appearance of new phases during cycling. Therefore, tuning both size and lattice disorder are effective methods for suppressing intercalation-induced phase transitions and introducing pseudocapacitive charge storage.

In this work, we highlighted the beneficial effects of disorder in nanostructured MoS₂, which serves as a model non-solid-solution system where we could reproducibly tune the amount of disorder due to the synthetic technique. As seen in previous studies on fast mixed-cation anode materials, disorder can suppress Li-ion ordering during intercalation by increasing the number of available intercalation sites at any given point during cycling. Decreased Li-ion ordering can also lead to the suppression of phase transitions. Controlling disorder in non-solid-solution materials is much more difficult, however, as it frequently results in poor cycling behavior. This is because, broadly, disorder can have both positive effects, like the decreased kinetic limitations from phase transitions that we highlight in this work, and negative ones, like slower Li⁺ diffusion due to poorly defined hopping pathways and loss of redox sites. The relative balance of these two effects determines whether disorder ends up as a net benefit. The importance of controlling competing effects of disorder can be seen clearly in layered oxide cathode materials, like NCA and NMC. In these compounds, transition metal disorder within the layers is essential to suppression of phase transitions, which is beneficial for rate capability, as we show here for MoS₂. However, antisite disorder, in which Li atoms switch places with transition metals in the crystal structure, impedes Li⁺ diffusion and harms performance. Clearly, not all disorder is beneficial, but specific kinds of disorder can be very synergistic with shortened diffusion lengths to achieve optimal rate capability. In cases where some lattice disorder does end up slowing diffusion, nanoscale size is also an effect way to mitigate those negative effects. One key conclusion of this work is that in systems without mixed heteroatom disorder, layer sliding and layer expansion can result in positive disorder effects and improved electrochemical performance. Overall, understanding the interplay between size and disorder in many electrode materials is key to harnessing their material properties toward fast-charging systems.

Acknowledgements

This work was supported by the US Department of Energy, Office of Basic Energy Sciences under Award Number DE-SC0014213. D.D.R. acknowledges support from a National Science Foundation Graduate Research Fellowship under award DGE-2034835. This research used resources of the Advanced Photon Source, a U.S. Department of Energy (DOE) Office of Science User Facility operated for the DOE Office of Science by Argonne National Laboratory under Contract No. DE-AC02-06CH11357. Beamline 11-ID-B and its mail-in program contributed to the data. The authors thank Andrey Yakovenko and Kamila Wiaderek for their advice and help during remote operations at APS due to the COVID-19 pandemic. The authors thank Prof. Simon J.L. Billinge for helpful discussions on the online diffpy user forum. The *operando* diffraction presented in this work was collected at the Stanford Synchrotron Radiation Lightsource, SLAC National Accelerator Laboratory, which is supported by the U.S. Department of Energy, Office of Science, Office of Basic Energy Sciences under Contract No. DE-AC02-76SF00515. The authors thank David Agyeman-Budu for help during limited operations at SSRL.

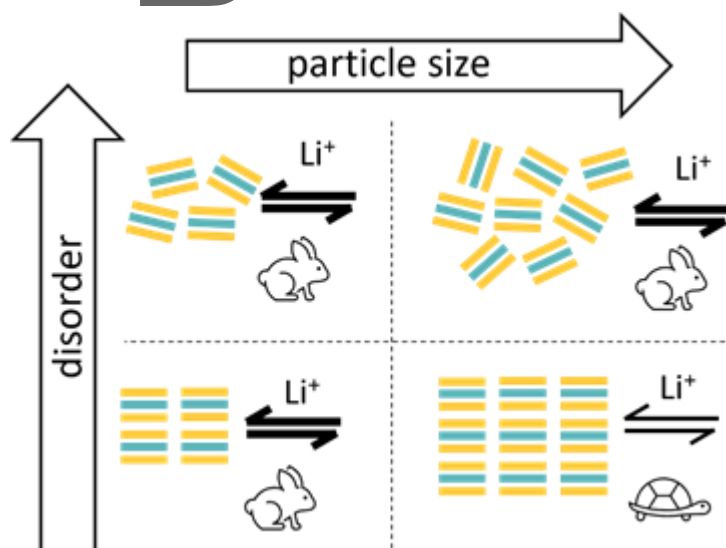
Received: ((will be filled in by the editorial staff))

Revised: ((will be filled in by the editorial staff))

Published online: ((will be filled in by the editorial staff))

Table of Contents Entry:

Fast charging lithium-ion batteries and pseudocapacitors can be created using nanostructured materials to produce short Li^+ -diffusion distances, combined with suppression of ion-insertion driven phase transitions. Such suppression can result from finite-size effects or the controlled introduction of disorder. Here, the interplay between size and disorder are studied in nanostructured MoS_2 . Both are found to facilitate fast charging, and they are complementary, with the fastest cycling found in small, disordered MoS_2 .

ToC figure:

This article is protected by copyright. All rights reserved.

References.

-
- ¹ Li, Matthew; Feng, Ming; Luo, Dan; Chen, Z. Fast Charging Li-Ion Batteries for a New Era of Electric Vehicles. *Cell Rep. Phys. Sci.* **2020**, *1*, 100212.
- ² Zhai, Y.; Dou, Y.; Zhao, D.; Fulvio, P. F.; Mayes, R. T.; Dai, S. Carbon Materials for Chemical Capacitive Energy Storage. *Adv. Mater.* **2011**, *23* (42), 4828–4850.
- ³ Simon, Patrice; Gogotsi, Yuri; Dunn, B. Where Do Batteries End and Supercapacitors Begin? *Science*, **2014**, *343*, 1210 – 1211.
- ⁴ Fleishmann, Simon; Mitchell, James B.; Wang, Ruocun; Zhan, Cheng; Jiang, De-en; Presser, Volker; Augustyn, V. Pseudocapacitance: From Fundamental Understanding to High Power Energy Storage Materials. *Chem. Rev.* **2020**, *120*, 6738 – 6782.
- ⁵ Wei, Q.; Chang, X.; Butts, D.; DeBlock, R.; Lan, K.; Li, J.; Chao, D.; Peng, D.-L.; Dunn, B. Surface-redox sodium-ion storage in anatase titanium oxide. *Nat. Commun.* **2023**, *14* (7).
- ⁶ Wei, Q.; Huang, T.; Huang, X.; Wang, B.; Jiang, Y.; Tang, D.; Peng, D.-L.; Dunn, B.; Mai, L. High-rate sodium-ion storage of vanadium nitride via surface-redox pseudocapacitance. *Interdiscip. Mater.* **2023**, *2*, 434 – 442.
- ⁷ Conway, B.E.; Pell, W.G. Double-layer and pseudocapacitance types of electrochemical capacitors and their applications to the development of hybrid devices. *J. SolidState Electrochem.* **2003**, *7*, 637 – 644.
- ⁸ Conway, B.E. Two-dimensional and quasi-two-dimensional isotherms for Li intercalation and up processes at surface. *Electrochim. Acta*, **1993**, *38*, 1249 – 1258.
- ⁹ Van der Ven, A.; Bhattacharya, J.; Belak, A. A. Understanding Li Diffusion in Li-Intercalation Compounds. *Acc. Chem. Res.* **2013**, *46*, 1216 – 1225.
- ¹⁰ Huang, H.; Niederberger, M. Towards Fast-Charging Technologies in Li⁺/Na⁺ Storage: From the Perspectives of Pseudocapacitive Materials and Non-Aqueous Hybrid Capacitors. *Nanoscale* **2019**, *11* (41), 19225–19240.
- ¹¹ Conway, B.E. *Electrochemical Supercapacitors: Scientific Fundamentals and Technological Applications*; Springer, 1999.
- ¹² Cook, J.B.; Kim, H.-S.; Lin, T.C.; Lai, C.-H.; Dunn, B.; Tolbert, S.H. Pseudocapacitive Charge Storage in Thick Composite MoS₂ Nanocrystal-Based Electrodes. *Adv. Energy Mater.* **2017**, *7*, 1601283.
- ¹³ Muller, G.A.; Cook, J.B.; Kim, H.-S.; Tolbert, S.H.; Dunn, B. High Performance Pseudocapacitor Based on 2D Layered Metal Chalcogenide Nanocrystals. *Nano Lett.* **2015**, *15*, 1911-1918.

- ¹⁴ Lesel, B.K.; Cook, J.B.; Yan, Y.; Lin, T.C.; Tolbert, S.H. Using Nanoscale Domain Size To Control Charge Storage Kinetics in Pseudocapacitive Nanoporous LiMn_2O_4 Powders. *ACS Energy Lett.* **2017**, *2*, 2293 – 2298.
- ¹⁵ Conway, B.E. Transition from ‘Supercapacitor’ to ‘Battery’ Behavior in Electrochemical Energy Storage. *J. Electrochem. Soc.* **1991**, *138*, 1539.
- ¹⁶ Okubo, M.; Hosono, E.; Kim, J.; Enomoto, M.; Kojima, N.; Kudo, T.; Zhou, H.; Honma, I. Nanosize Effect on High-Rate Li-Ion Intercalation in LiCoO_2 Electrode. *J. Am. Chem. Soc.* **2007**, *129*, 7444 – 7452.
- ¹⁷ Kim, H.-S.; Cook, J.B.; Tolbert, S.H.; Dunn, V. The Development of Pseudocapacitive Properties in Nanosized- MoO_2 . *J. Electrochem. Soc.* **2015**, *162*, A5083 – A5090.
- ¹⁸ Yan, Y.; Chin, M.A.; Robertson, D.D.; Lesel, B.K.; Tolbert, S.H. Tuning the Porous Structure in PMMA-Templated Mesoporous MoO_2 for Pseudocapacitive Li-ion Electrodes. *J. Electrochem. Soc.* **2022**, *169*, 4, 040545.
- ¹⁹ Fleischmann, S.; Shao, H.; Taberna, P.L.; Rozier, P.; Simon, P. Electrochemically Induced Deformation Determines the Rate of Lithium Intercalation in Bulk TiS_2 . *ACS Energy Lett.* **2021**, *6* (12), 4173–4178.
- ²⁰ Cook, J.B.; Lin, T.C.; Kim, H.-S.; Siordia, A.; Dunn, B.S.; Tolbert, S.H. Suppression of Electrochemically Driven Phase Transitions in Nanostructured MoS_2 Pseudocapacitors Probed Using Operando X-ray Diffraction. *ACS Nano*, **2019**, *13*, 1223–1231.
- ²¹ Cook, J.B.; Ko, J.S.; Lin, T.C.; Robertson, D.D.; Kim, H.-S.; Yan, Y.; Yao, Y. Dunn, B.S.; Tolbert, S.H. Ultrafast Sodium Intercalation Pseudocapacitance in MoS_2 Facilitated by Phase Transition Suppression. *ACS Appl. Energy Mater.* **2023**, *6* (1), 99–108.
- ²² Bai, P.; Cogswell, D.A.; Bazant, M.Z. Suppression of Phase Separation in LiFePO_4 Nanoparticles During Battery Discharge. *Nano Lett.* **2011**, *11*, 4890 – 4896.
- ²³ Zhang, X.; van Hulzen, M.; Singh, D.P.; Brownrigg, A.; Wright, J.P.; van Dijk, N.H.; Wagemaker, M. Rate-induced Solubility and Suppression of the First-Order Phase Transition in Olivine LiFePO_4 . *Nano Lett.* **2014**, *14*, 2279 – 2285.
- ²⁴ Xu, Y.; Wang, Z.; Yang, Z.; Na, J.; Azhar, A.; Wang, S.; Yu, J.; Yamauchi, Y. New Insights into the Lithium-Ion Diffusion Mechanism in Vanadate Compounds. *ACS Energy Lett.* **2021**, *6*, 886–892.
- ²⁵ Wu, M.; Xu, B.; Ouyang, C. Physics of electron and lithium-ion transport in electrode materials for Li-ion batteries. *Chin. Phys. B* **2016**, *25*, 018206.
- ²⁶ Koçer, C.P.; Griffith, K.J.; Grey, C.P., Morris, A.J. Cation Disorder and Lithium Insertion Mechanism of Wadsley–Roth Crystallographic Shear Phases from First Principles. *J. Am. Chem. Soc.* **2019**, *141*, 15121–15134.
- ²⁷ Griffith, K.J.; Wiaderek, K.M.; Cibir, G.; Marbella, L.E.; Grey, C.P. Niobium tungsten oxides for high-rate lithium-ion energy storage. *Nature* **2018**, *559* (7715), 556–563.

This article is protected by copyright. All rights reserved.

- ²⁸ Yang, Y.; Zhu, H.; Xiao, J.; Geng, H.; Zhang, Y.; Zhao, J.; Li, G.; Wang, X.-L.; Li, C.C.; Liu, Q. Achieving Ultrahigh-Rate and High-Safety Li⁺ Storage Based on Interconnected Tunnel Structure in Micro-Size Niobium Tungsten Oxides. *Adv. Mater.* **2020**, *32* (12), 1905295.
- ²⁹ Ohno, S.; Helm, B.; Fuchs, T.; Dewald, G.; Kraft, M.A.; Culver, S.P.; Senyshyn, A.; Zeier, W.G. Further Evidence for Energy Landscape Flattening in the Superionic Argyrodites Li_{6+x}P_{1-x}M_xS₅I (M = Si, Ge, Sn). *Chem. Mater.* **2019**, *31*, 4936–4944.
- ³⁰ Zhang, Y.; Zhao, Y.; Chen, C. *Ab initio* study of the stabilities of and mechanism of superionic transport in lithium-rich antiperovskites. *Phys. Rev. B.* **2013**, *87*, 134303.
- ³¹ Robert, R.; Bünzli, C.; Berg, E.J.; Novák, P. Activation Mechanism of LiNi_{0.80}Co_{0.15}Al_{0.05}O₂: Surface and Bulk Operando Electrochemical, Differential Electrochemical Mass Spectrometry, and X-ray Diffraction Analyses. *Chem. Mater.* **2015**, *27*, 526 – 536.
- ³² Purwanto, A.; Yudha, C.S.; Ubaidillah, U.; Widiyandari, H.; Ogi, T.; Haerudin, H. NCA cathode material: synthesis methods and performance enhancement efforts. *Mater. Res. Express*, **2019**, *5*, 122001.
- ³³ Moshtev, R.V.; Zlatilova, P.; Manev, V.; Sato, A. The LiNiO₂ solid solution as a cathode material for rechargeable lithium batteries. *J. Power Sources* **1995**, *54*, 329 – 333.
- ³⁴ Biasi, L.; Schiele, A.; Roca-Ayats, M.; Garcia, G.; Brezesinski, T.; Hartmann, P.; Janek, J. Phase Transformation Behavior and Stability of LiNiO₂ Cathode Material for Li-Ion Batteries Obtained from In Situ Gas Analysis and Operando X-Ray Diffraction. *ChemSusChem*, **2019**, *12*, 2240 – 2250.
- ³⁵ Castro-García, S.; Castro-Coucerio, A.; Señarís-Rodríguez, M.A.; Soulette, F.; Julien, C. Influence of aluminum doping on the properties of LiCoO₂ and LiNi_{0.5}Co_{0.5}O₂ oxides. *Solid State Ion.* **2003**, *156*, 15 – 26.
- ³⁶ Kim, H.-S.; Cook, J.B.; Lin, H.; Ko, J.S.; Tolbert, S.H.; Ozolins, V.; Dunn, B. Oxygen vacancies enhance pseudocapacitive charge storage properties of MoO_{3-x}. *Nat. Mater.* **2017**, *16*, 454 – 460.
- ³⁷ Liu, X.; Wang, Y.; Yang, Y.; Lv, W.; Lian, G.; Golberg, D.; Wang, X.; Zhao, X.; Ding, Y. A MoS₂/Carbon hybrid anode for high-performance Li-ion batteries at low temperature. *Nano Energy*, **2020**, *70*, 104550.
- ³⁸ Shan, T.-T.; Xin, S.; You, Y.; Cong, H.-P.; Yu, S.-H.; Manthiram, A. Combining Nitrogen-Doped Graphene Sheets and MoS₂: A Unique Film-Foam-Film Structure for Enhanced Lithium Storage. *Angew. Chem. Int. Ed.*, **2016**, *55*, 12783-12788.
- ³⁹ Liu, Y.; Zhang, L.; Wang, H.; Yu, C.; Yan, X.; Liu, Q.; Xu, B.; Wang, L.-M. Synthesis of severe lattice distorted MoS₂ coupled with hetero-bonds as anode for superior lithium-ion batteries. *Electrochim. Acta*, **2018**, *262*, 162-172.
- ⁴⁰ Stephenson, T.; Li, Z.; Olsen, B.; Mitlin, D. Lithium ion battery applications of molybdenum disulfide (MoS₂) nanocomposites. *Energy Environ. Sci.* **2014**, *7*, 209-231.

- ⁴¹ Huang, X.; Zeng, Z.; Zhang, H. Metal dichalcogenide nanosheets: preparation, properties and applications. *Chem. Soc. Rev.* **2013**, *42*, 1934–1946.
- ⁴² Huang, G.; Chen, T.; Chen, W.; Wang, Z.; Chang, K.; Ma, L.; Huang, F.; Chen, D.; Lee, J.Y. Graphene-Like MoS₂/Graphene Composites: Cationic Surfactant-Assisted Hydrothermal Synthesis and Electrochemical Reversible Storage of Lithium. *Small*, **2013**, *9*, 3693–3703.
- ⁴³ Quilty, C. D.; Housel, L. M.; Bock, D. C.; Dunkin, M. R.; Wang, L.; Lutz, D. M.; Abraham, A.; Bruck, A. M.; Takeuchi, E. S.; Takeuchi, K. J.; Marschilok, A. C. Ex Situ and Operando XRD and XAS Analysis of MoS₂: A Lithiation Study of Bulk and Nanosheet Materials. *ACS Appl. Energy Mater.* **2019**, *2* (10), 7635–7646.
- ⁴⁴ Lutz, D. M.; Dunkin, M. R.; King, S. T.; Stackhouse, C. A.; Kuang, J.; Du, Y.; Bak, S. M.; Bock, D. C.; Tong, X.; Ma, L.; Ehrlich, S. N.; Takeuchi, E. S.; Takeuchi, K. J.; Marschilok, A. C.; Wang, L. Hybrid MoS_{2+x} Nanosheet/Nanocarbon Heterostructures for Lithium-Ion Batteries. *ACS Appl. Nano Mater.* **2022**, *5* (4), 5103–5118.
- ⁴⁵ Zhang, X.; An, C.; Wang, S.; Wang, Z.; Xia, D. Green synthesis of metal sulfide nanocrystals through a general composite-surfactants-aided-solvothermal process. *J. Cryst. Growth.* **2009**, *311*, 3775–3780.
- ⁴⁶ Liu, H.; Su, D.; Zhou, R.; Sun, B.; Wang, G.; Qiao, S.Z. Highly Ordered Mesoporous MoS₂ with Expanded Spacing of the (002) Crystal Plane for Ultrafast Lithium Ion Storage. *Adv. Energy Mater.* **2012**, *2*, 970–975.
- ⁴⁷ Zhang, C.; Wu, H.B.; Guo, Z.; Lou, X.W. Facile synthesis of carbon-coated MoS₂ nanorods with enhanced lithium storage properties". *Electrochem. Commun.* **2012**, *20*, 7–10.
- ⁴⁸ Hu, X.; Zhang, W.; Liu, X.; Mei, Y.; Huang, Y. Nanostructured Mo-based electrode materials for electrochemical energy storage. *Chem. Soc. Rev.* **2015**, *44*, 2376–2404.
- ⁴⁹ Cook, J.B.; Kim, H.-S.; Yan, Y.; Ko, J.S.; Robbennolt, S.; Dunn, B.; Tolbert, S.H. Mesoporous MoS₂ as a Transition Metal Dichalcogenide Exhibiting Pseudocapacitive Li and Na-Ion Charge Storage. *Adv. Energy Mater.* **2016**, *6*, 1–12.
- ⁵⁰ Wu, J.; Dai, J.; Shao, Y.; Cao, M.; Wu, X. Carbon dot-assisted hydrothermal synthesis of flower-like MoS₂ nanospheres constructed by few-layered multiphase MoS₂ nanosheets for supercapacitors. *RSC Adv.* **2016**, *6*, 77999–78007.
- ⁵¹ Fang, L.; Qiu, Y.; Li, W.; Wang, F.; Lan, M.; Huang, K.; Jing, Q. Three-dimensional flower-like MoS₂-CoSe₂ heterostructure for high performance supercapacitors. *J. Colloid Interface Sci.* **2018**, *512*, 282–290.
- ⁵² Fang, X.; Hua, C.; Guo, X.; Hu, Y.; Wang, Z.; Gao, X.; Wu, F.; Wang, J.; Chen, L. Lithium storage in commercial MoS₂ in different potential ranges. *Electrochim. Acta*, **2012**, *81*, 155–160.
- ⁵³ Abraham, A.; Wang, L.; Quilty, C. D.; Lutz, D. M.; McCarthy, A. H.; Tang, C. R.; Dunkin, M. R.; Housel, L. M.; Takeuchi, E. S.; Marschilok, A. C.; Takeuchi, K. J. Defect Control in the Synthesis of 2D

MoS₂ Nanosheets: Polysulfide Trapping in Composite Sulfur Cathodes for Li-S Batteries. *ChemSusChem* **2020**, *13* (6), 1517–1528.

⁵⁴ Jin, Q.; Liu, N.; Chen, B.; Mei, D. Mechanisms of Semiconducting 2H to Metallic 1T Phase Transition in Two-dimensional MoS₂ Nanosheets. *J. Phys. Chem. C* **2018**, *122*, 28215–28224.

⁵⁵ Gan, X.; Lee, L.Y.S.; Wong, K.-Y.; Lo, T.W.; Ho, K.H.; Lei, D.Y.; Zhao, H. 2H/1T Phase Transition of Multilayer MoS₂ by Electrochemical Incorporation of S Vacancies. *ACS Appl. Energy Mater.* **2018**, *1*, 4754–4765.

⁵⁶ Wypych, F.; Schöllhorn, R. 1T-MoS₂, a New Metallic Modification of Molybdenum Disulfide. *J. Chem. Soc., Chem. Commun.* **1992**, 1386–1388.

⁵⁷ Goloveshkin, A.S.; Bushmarinov, I.S.; Korlyukov, A.A.; Buzin, M.I.; Zaikovskii, V.I.; Lenenko, N.D.; Golub, A.S. Stabilization of 1T-MoS₂ Sheets by Imidazolium Molecules in Self-Assembling Hetero-layered Nanocrystals. *Langmuir*, **2015**, *31*, 8953–8960.

⁵⁸ Py, M.A.; Haering, R.R. Structural destabilization induced by lithium intercalation in MoS₂ and related compounds. *Can. J. Phys.* **1983**, *61*, 76–84.

⁵⁹ Mattheiss, L.F. Band Structures of Transition-Metal-Dichalcogenide Layer Compounds. *Phys. Rev. B*, **1973**, *8*, 3719–3740.

⁶⁰ Wang, T.; Sel, O.; Djerdj, I.; Smarsly, B. Preparation of a large Mesoporous CeO₂ with crystalline walls using PMMA colloidal crystal templates. *Colloid Polym. Sci.* **2006**, *285*, 1–9.

⁶¹ Nagabhushana, G.P.; Samrat, D.; Chandrappa, G.T. α-MoO₃ nanoparticles: solution combustion synthesis, photocatalytic and electrochemical properties. *RSC Adv.* **2014**, *4*, 56784.

⁶² Toby, B.H. and R.B. Von Dreele. GSAS-II: the genesis of a modern open-source all purpose crystallography software package. *J. Appl. Crystallogr.* **2013**, *46*, 544 – 549.

⁶³ Farrow, C.L.; Juhas, P.; Liu, J.W.; Bryndin, D.; Bozin, E.S.; Block, J.; Proffen, Th.; and S.J.L. Billinge. PDFfit2 and PDFgui: computer programs for studying nanostructure in crystals. *J. Phys.: Condens. Mat.*, **2007**, *19*, 335219.

⁶⁴ Schonfeld, B.; Huang, J.J.; Moss, S. C. Anisotropic mean-square displacements (MSD) in single crystals of 2H- and 3R-MoS₂. *Acta. Crystallogr. B. Struct. Sci. Cryst.* **1983**, *39*, 404 – 407.

⁶⁵ Petkov, V.; Vogt, T.; Billinge, S.J.L.; Mahanti, S.D.; Larson, P.; Rangan, K.K.; Kanatzidis, M.G. Structure of nanocrystalline materials using atomic pair distribution function analysis: study of LiMoS₂. *Phys. Rev. B* **2002**, *65*, 921051 – 921054.

⁶⁶ Jain, A.; Ong, S.P.; Hautier, G.; Chen, W.; Richards, W.D.; Dacek, S.; Cholia, S.; Gunter, D.; Skinner, D.; Ceder, G.; Persson, K.A. Commentary: The Materials Project: A materials genome approach to accelerating materials innovation. *APL Mater.* **2013**, *1*, 011002.

- ⁶⁷ Wang, J.; Zhang, L.; Sun, K.; He, J.; Zheng, Y.; Xu, C.; Zhang, Y.; Chen, Y.; Li, M. Improving Ionic/Electronic Conductivity of MoS₂ Li-Ion Anode via Manganese Doping and Structural Optimization. *Chem. Eng. J.* **2019**, *372*, 665–672.
- ⁶⁸ Remskar, M.; Mrzel, A.; Virsek, M.; Godec, M.; Krause, M.; Kolitsch, A.; Singh, A.; Seabaugh, A. The MoS₂ Nanotubes with Defect-Controlled Electric Properties." *Nanoscale Res. Lett.* **2011**, *6*, 1 – 6.
- ⁶⁹ Wang, X.; Tan, S.; Yang, X.-Q.; Hu, E. Pair distribution function analysis: Fundamentals and application to battery materials. *Chin. Phys. B*, **2020**, *29*, 028802.
- ⁷⁰ Keen, D.A. A comparison of various commonly used correlation functions for describing total scattering. *J. Appl. Crystallogr.* **2001**, *34*, 172 – 177.
- ⁷¹ Chapman, K.W. Emerging *operando* and x-ray pair distribution function methods for energy materials development. *MRS Bull.* **2016**, *41*, 231 – 238.
- ⁷² Voiry, D.; Mohite, A.; Chhowalla, M. Phase engineering of transition metal dichalcogenides. *Chem. Soc. Rev.* **2015**, *44*, 2702 – 2712.
- ⁷³ Strachan, J.; Masters, A.F.; Maschmeyer, T. 3R-MoS₂ in Review: History, Status, and Outlook. *ACS Appl. Energy Mater.* **2021**, *4*, 7405 – 7418.
- ⁷⁴ Guo, B.; Yu, X.; Sun, X.G.; Chi, M.; Qiao, Z.A.; Liu, J.; Hu, Y.S.; Yang, X.Q.; Goodenough, J.B.; Dai, S. A long-life lithium-ion battery with a highly porous TiNb₂O₇ anode for large-scale electrical energy storage. *Energy Environ. Sci.* **2014**, *7* (7), 2220-2226.
- ⁷⁵ Yi, T.F.; Yang, S.Y.; Xie, Y. Recent advances of Li₄Ti₅O₁₂ as a promising next generation anode material for high power lithium-ion batteries. *J. Mater. Chem. A* **2015**, *3* (11), 5750-5777.
- ⁷⁶ Griffith, K.J.; Seymour, I.D.; Hope, M.A.; Butala, M.M.; Lamontagne, L.K.; Preefer, M.B.; Koçer, C.P.; Henkelman, G.; Morris, A.J.; Cliffe, M.J.; Dutton, S.E.; Grey, C.P. Ionic and Electronic Conduction in TiNb₂O₇. *J. Am. Chem. Soc.* **2019**, *141* (42), 16706-16725.
- ⁷⁷ Preefer, M.B.; Saber, M.; Wei, Q.; Bashian, N.H.; Bocarsly, J.D.; Zhang, W.; Lee, G.; Milam-Guerrero, J.; Howard, E.S.; Vincent, R.C.; Melot, B.C.; Van der Ven, A.; Seshadri, R.; Dunn, B. Multielectron Redox and Insulator-to-Metal Transition upon Lithium Insertion in the Fast-Charging, Wadsley-Roth Phase PNB₉O₂₅. *Chem. Mater.* **2020**, *32* (11), 4553-4563.
- ⁷⁸ Downie, L.E.; Krause, L.J.; Burns, J.C.; Jensen, L.D.; Chevrier, V.L.; Dahn, J.R. In Situ Detection of Lithium Plating on Graphite Electrodes by Electrochemical Calorimetry. *J. Electrochem. Soc.* **2013**, *160* (4), A588.
- ⁷⁹ Liu, Y.; Zhu, Y.; Cui, Y. Challenges and opportunities towards fast-charging battery materials. *Nat. Energy* **2019**, *4* (7), 540-550.
- ⁸⁰ Bard, A.J. and Larry R. Faulkner. *Electrochemical Methods: Fundamentals and Applications*; John Wiley & Sons, Inc, 1980.

- ⁸¹ Lindström, H.; Södergren, S.; Solbrand, A.; Rensmo, H.; Hjelm, J.; Hagfeldt, A.; Lindquist, S.-E. Li⁺ Ion Insertion in TiO₂ (Anatase). 2. Voltammetry on Nanoporous Films. *J. Phys. Chem. B* **1997**, *101*, 7717-7722.
- ⁸² Liu, T.-C.; Pell, W.G.; Conway, B.E. Behavior of Molybdenum Nitrides as Materials for Electrochemical Capacitors: Comparison with Ruthenium Oxide. *J. Electrochem. Soc.* **1998**, *145*, 1882-1888.
- ⁸³ Wepper, W.; Huggins, R.A. Determination of the Kinetic Parameters of Mixed-Conducting Electrodes and Application to the System Li₃Sb. *J. Electrochem. Soc.* **1977**, *124*, 1569-1578.
- ⁸⁴ Verma, A.; Smith, K.; Santhanagopalan, S.; Abraham, D.; Yao, K.P.; Mukherjee, P.P. Galvanostatic Intermittent Titration and performance Based Analysis of LiNi_{0.5}Co_{0.2}Mn_{0.3}O₂ Cathode. *J. Electrochem. Soc.* **2017**, *164*, 3380-3392.
- ⁸⁵ Zou, J.; Li, F.; Bissett, M.A.; Kim, F.; Hardwick, L.J. Intercalation behavior of Li and Na into 3-layer and multilayer MoS₂ flakes. *Electrochim. Acta*, **2020**, *331*, 135284.
- ⁸⁶ Nickol, A.; Schied, T.; Heubner, C.; Schneider, M.; Michaelis, A.; Bobeth, M.; Cuniberti, G. GITT Analysis of Lithium Insertion Cathodes for Determining the Lithium Diffusion Coefficient at Low Temperature: Challenges and Pitfalls. *J. Electrochem. Soc.* **2020**, *167*, 090546.
- ⁸⁷ Zhu, Y.; Wang, C. Galvanostatic Intermittent Titration Technique for Phase-Transformation Electrodes. *J. Phys. Chem. C*, **2010**, *114*, 2830-2841.
- ⁸⁸ Wang, G.; Zhang, Y.; Cho, H. S.; Zhao, X.; Kim, F.; Zou, J. Revisiting the Structural Evolution of MoS₂ during Alkali Metal (Li, Na, and K) Intercalation. *ACS Appl. Energy Mater.* **2021**, *4* (12), 14180-14190.
- ⁸⁹ Huang, L.; Wei, Q.; Xu, X.; Shi, C.; Liu, X.; Zhou, L.; Mai, L. Methyl-functionalized MoS₂ nanosheets with reduced lattice breathing for enhanced pseudocapacitive sodium storage. *Phys. Chem. Chem. Phys.* **2017**, *19*, 13696 - 13702.